ATTITUDE SENSOR STUDY

Prepared under Contract No. NAS 3-2510 by

HUGHES RESEARCH LABORATORIES

Malibu, California

for

NATIONAL AERONAUTICS AND SPACE ADMINISTRATION

TABLE OF CONTENTS

LIST OF FIGURES

LIST OF FIGURES

(contd.)

vi

LIST OF FIGURES

(contd.)

I. INTRODUCTION AND SUMMARY

A. Program Objectives

The ion rocket engine system for attitude control and station keeping of a synchronous orbit satellite is presently being developed by Hughes Aircraft Company under NASA contract NAS 3-2510. This program has as an objective the development of a satellite control system utilizing ion engine propulsion to provide attitude control torques and orbit control impulses.

During the development of the control system it has become evident that the early definition of the attitude sensors required for system operation was imperative to assure compatibility of the system design with the obtainable sensor characteristics. Such factors as sensor output noise and null accuracy have a direct and important bearing in ascertaining adequacy of the selected control system performance. Because of these considerations, a survey of attitude sensors has been conducted with the objective of selecting a suitable sensor subsystem for the ion engine control system.

Early in the survey it became apparent that the sensor requirements for the synchronous orbit mission were not compatible with those of the low altitude test mission in which the ion engine control system will initially be flight tested. A sensor subsystem consisting of a two-axis sun sensor and a single-axis earth sensor has been recommended for the polar orbit mission to provide a sun oriented stabilization of the vehicle attitude. The detail reasons for this recommendation and descriptions of the selected sensors are presented in Reference 1.

The requirements for the synchronous orbit mission sensor subsystem and analysis of instruments suitable for this application have been the subject of additional study with the objective of selecting attitude sensors for this mission.

In conjunction with the sensor survey, analog computer simulation studies have been conducted to determine adequacy of the attitude control system performance when non-ideal sensor error signal characteristics are simulated. This study includes evaluation of the effects of sensor noise, null shift, and gain variation on system performance. Effects of disturbance torques on the limit cycle system operation have also been investigated.

B.   Control System Description

Attitude control torques are obtained by the use of four pairs of linear strip ion engines, with each engine producing 0.5 millipound of thrust. Each pair of engines are mounted back to back at the end of a moment arm, which is normal to the controlled axis, with the thrust vectors collinear and oppositely directed.

The orientation of the four pairs of attitude control engines is shown in Figure 1 with the attitude control thrust vectors designated as N_1, N_2, E_1, E_2, S_1, S_2, W_1, W_2.

Four pairs of engines are employed with a positioning mechanism to provide 100 percent redundancy of the attitude control and station keeping functions. The positioner rotates the thrust vectors 90 degrees to the alternate orientation if a failure occurs in the primary control mode. The North, East, and West engine pairs comprise the primary system to provide control torques about the roll, yaw, and pitch axes, respectively.

The station keeping function of the mission is provided for by annular strip ion engines producing 1.5 millipound thrust through the satellite center of gravity. Each of these engines is combined with a pair of attitude control engines and a central cesium feed system into an engine station package. The station keeping engines thrust in the plane of the orbit or normal to the plane to provide longitudinal and latitudinal control ot the satellite position. Thrusting of the appropriate engine is controlled by ground command to maintain the satellite position within $\pm$ 0.1 degree latitude and longitude of the desired location.

2
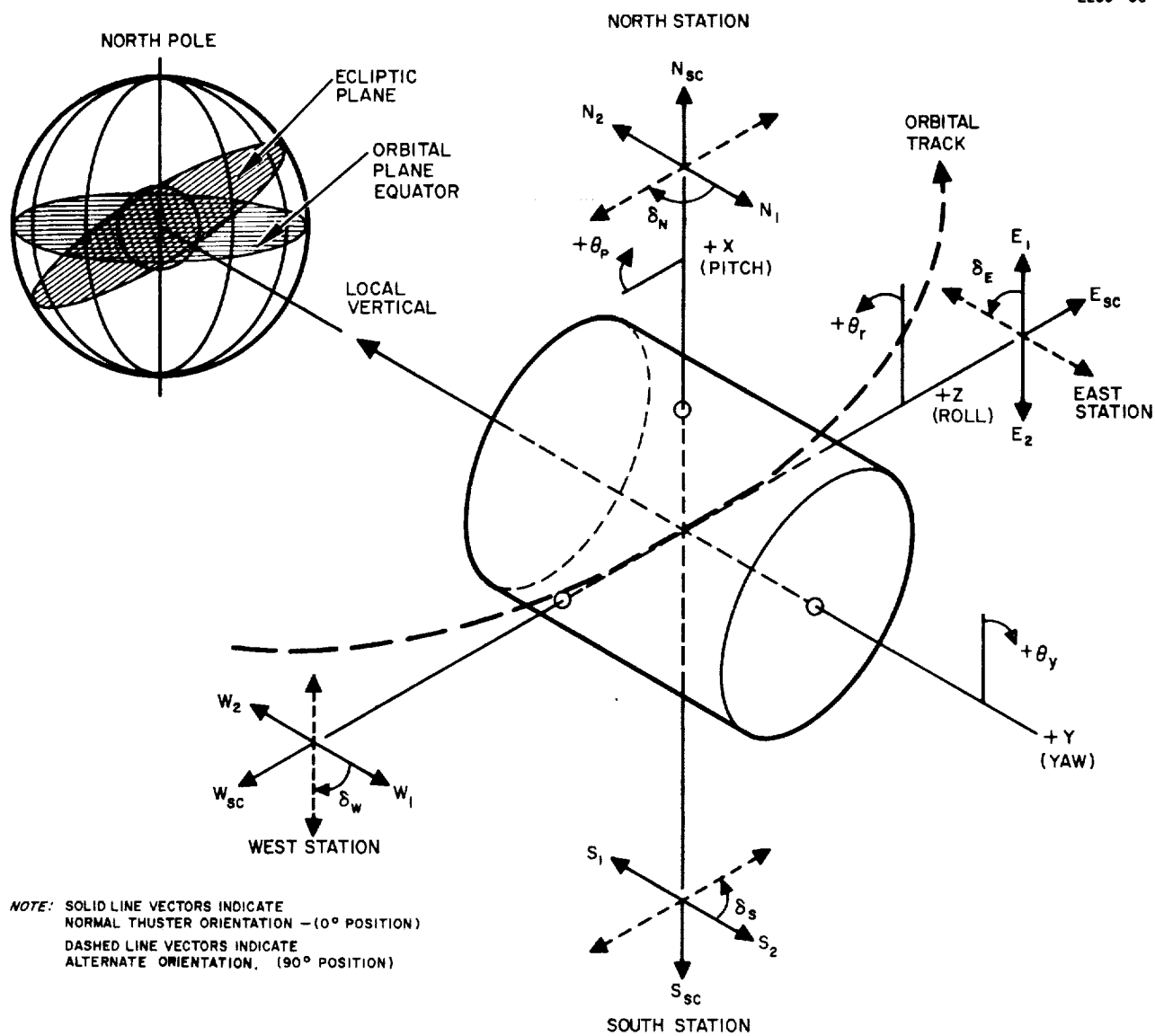
Fig. 1.   Thrust vector orientation.

3

The attitude control system is designed to maintain the pitch and roll axis normal to the local vertical within ± 0.5 degree and to stabilize yaw about the local vertical to within ± 0.5 degree. The system requires linear attitude error signals from the attitude sensor subsystem. These signals are shaped in lead-lag networks and applied to deadband switches to control initiation or termination of engine thrusting. The system functional block diagram for the primary system mode is illustrated in Figure 2. Control switching logic is employed between the deadband switch output and the engine station inputs to provide switching of the thrust command signals to appropriate thrustors for control redundancy.

C.   Report Content Summary

This report is presented in two major sections, the first of which deals with the sensor survey study and the second section presents the results of the system simulation study.

The sensor subsystem requirements are evaluated to determine constraints on the attitude sensors imposed by the control system design, mission requirements and the orbital geometry. Available reference systems for attitude sensors are evaluated to ascertain the suitability of the system and associated instruments. A detail analysis of the most suitable sensor instruments is presented and recommendations are made for selection of a sensor subsystem consisting of earth and star sensors.

The system simulation section of this report is subdivided into two parts, the first of which presents the final system simulation results; the second part presents the results of the synchronous orbit system simulation.

A description of the simulation program is given for each system and the range of variables utilized in the study is presented. The results, presented in graphical form and phase plane representation of system performance, indicate acceptable operation of the control system for the expected variation of sensor characteristics.

4
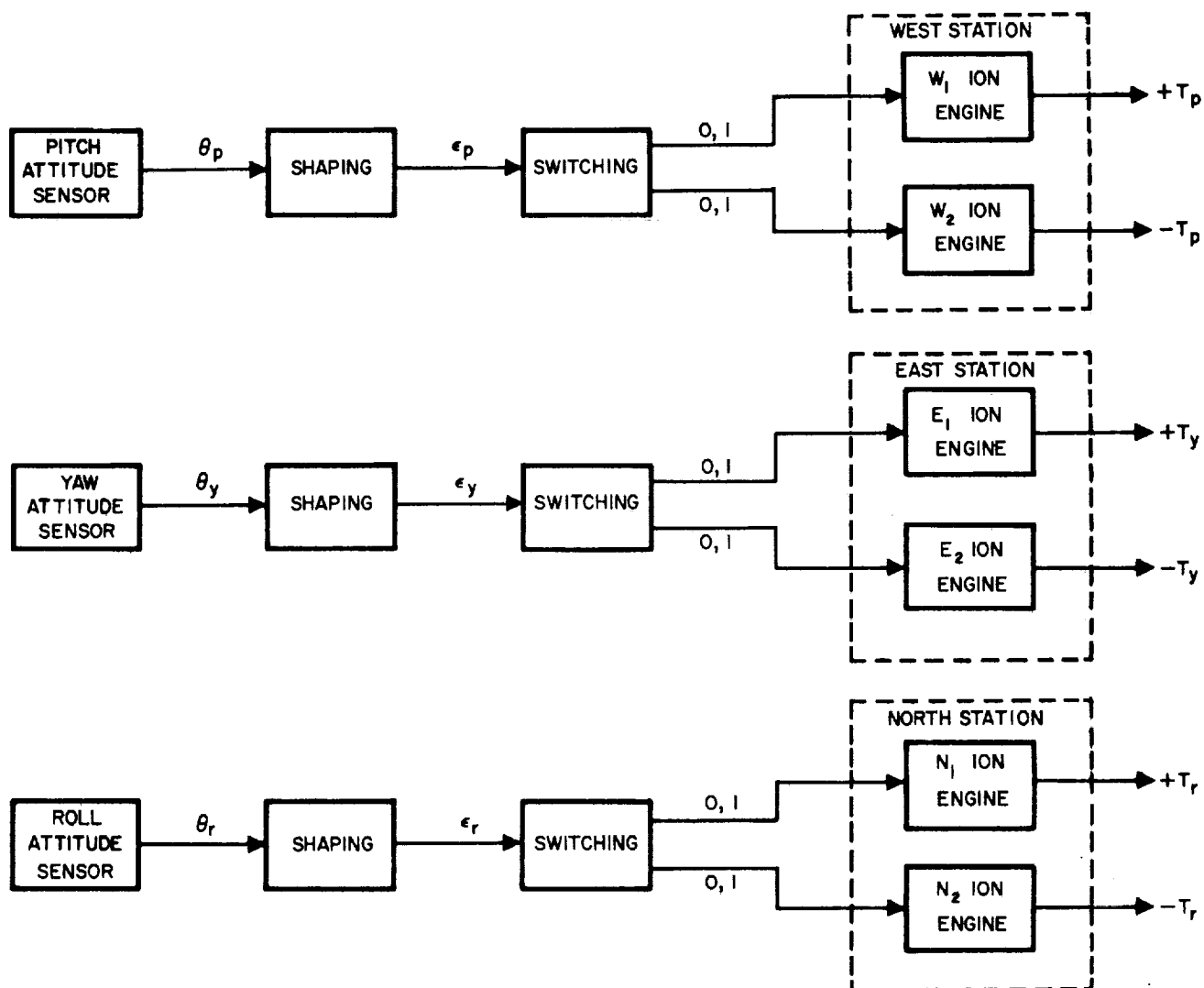
Fig. 2. Control system functional block diagram.

II.   ATTITUDE SENSOR SURVEY

A.   Sensor Subsystem Requirements

The sensor subsystem is required to furnish attitude error signals proportional to the angular deviation of the vehicle-fixed coordinate system from an earth-oriented reference coordinate system. The reference frame illustrated in Figure 1 is oriented with the roll axis lying in the orbital plane and perpendicular to the local vertical. The yaw axis is parallel to the local vertical and the pitch axis is orthogonal to the roll and yaw axes. A constant angular rate equal to the orbital rate (ω = 0.0042 deg/sec) of the spacecraft is initially set into the vehicle about the pitch axis to maintain earth orientation of the reference frame.

The ion engine attitude control system functions to limit the angular deviation of the vehicle-fixed axes from the reference frame to a maximum of $\pm$0.5 degree. Since any inaccuracy in the sensor system results in increased uncertainty of the vehicle attitude, the sensor should be capable of less than 0.1 degree null accuracy.

Sensor output signal drift or long-term signal variation not resulting from an attitude change will cause increased power consumption, since the control duty cycle is effectively increased. Any such drift inherent in a sensor design must be limited to an order of magnitude less than the limit cycle angular rate of 0.003 deg/sec.

Useful linear range of the sensor must include the design attitude deadband ($\pm$0.5 degree) of the control system plus some margin to provide limited initial acquisition capability. Analysis has shown that use of the ion engine control system in the limit cycle mode to remove initial vehicle tumbling rates is not practical because of the low control torque-to-inertia ratio. Therefore, wide linear range of the sensors is not required. A linear range of $\pm$ 3 degrees will permit vehicle angular rates of 0.04 degree per second upon initiation of limit cycle control without sensor saturation. This initial rate is obtainable by the use of a rate

nulling system in which an attitude control ion engine would thrust to null out an error signal from a rate gyro in each axis.

Linearity requirements on the sensor error signal are not clearly bound and have been arbitrarily set at $\pm$ 10 percent.

The required sensor scale factor has been established at 2 volts per degree by the design of the control electronics, which has a d-c gain of 2.5 and a deadband switching level of 2.5 volts. The circuit parameters have been selected to minimize signal drift with component temperature rate of change while providing the required shaping amplifier dynamic range and switch hysteresis with the selected voltages and components.

The attitude sensor output signal noise and time constant are inter-related and must be considered together as to their effect on system operation. It is desirable to maintain a sensor time constant of less than 0.1 second to avoid the destabilizing effect of additional system lag; however, as shown in Reference 1, a larger time constant is acceptable at the sacrifice of additional power consumption.

Sensor noise output is amplified by the lead-lag shaping amplifier and applied to the deadband switches. When the peak-to-peak noise value exceeds the 0.1 volt switch hysteresis level, chattering will occur when the signal plus noise turns on the switch. This chattering results in reliability problems in the ion engine power control circuitry and thermal shock of the engine ionizer assembly. To preclude such problems, the sensor output noise must be restricted and a modification to the deadband switch (switch kick) has been designed.

Without the switch modification, sensor white noise over a 35 cps bandwidth must be limited to approximately 8 millivolts. The switch kick modification, which lowers the switch-off level whenever the switch is turned on, increases the allowable noise by a factor of 3 for a practical circuit design. Addition of lag filtration further

increases allowable noise at the expense of additional power consumption as shown in Section III of this report. Allowable single frequency noise is approximated by a value in millivolts equal to 5 times the frequency for the unmodified switch.

Environmental exposure requirements for the sensors are incomplete because of the undefined launch vehicle for the synchronous orbit satellite; however, typical values of boost dynamic environment and expected sensor operating temperature range are listed in Table I with the required sensor error signal characteristics. Arbitrary maximum desired values of sensor weight, power, and volume are also tabulated.

A major consideration in evaluation of sensor systems for this application is the reliability requirement associated with the 3-year operational life specified for the control system. Sensor instrument designs which include mechanical elements subject to wear are undesirable since prediction of operating life is difficult and reliability testing is impractical.

TABLE I

ATTITUDE SENSOR
PRELIMINARY DESIGN SPECIFICATION

Item	Characteristics	Required Value
1.	Null accuracy (degrees)	± 0.1
2.	Allowable null drift rate (deg/sec)	10^{-4} maximum
3.	Useful linear range (degrees)	± 3
4.	Linearity in linear range (percent)	10
5.	Scale factor (volts d.c./degree)	2
6.	Signal time constant (time in seconds for output signal to rise to 63 percent of final value in response to a step change in apparent star position of 0.25 degree)	0.1 maximum
7.	Sensor noise output (millivolts, rms)	
	(a) Single frequency at "f" cps (e.g. allowable noise at 25 cps = 125 mv, rms)	5 "f" maximum
	(b) White noise out to 35 cps	6 maximum
NOTE:	If no appreciable single frequency noise is present, white noise limit is 8 maximum.	
8.	Environmental Conditions	
	Operational Exposures:	
	Temperature range:	0 to 120° F
	Vacuum:	10^{-13} mm Hg
	Survival Exposures:	
	Acceleration:	35 g continuous
	Shock:	60 g peak, 5μsec rise
	Vibration:	20-2000 cps sinusoidal 15 g rms 20-2000 cps random (Gaussian) 12 g rms

Item	Characteristics	Required Value
9.	Power Required, continuous (watts)	10 maximum
10.	Weight (pounds)	8 maximum
11.	Displacement (cubic inches)	500 maximum
12.	Operating life (years)	3 minimum
13.	Voltages available: Unregulated $\pm 10\%$ d.c. in the range 24 to 35 volts. Single phase a.c., 400 cps 26 volts peak	
14.	Output characteristics: Two wire differential output signal. Impedance presented to above signal is 750 K ohms line to line	

B.   Available Attitude Reference Systems

The reference systems available for attitude sensors may be categorized into (1) inertial space, (2) ambient field potentials, (3) observation of celestial bodies, and (4) detection of earth-emitted or reflected radiation. Factors affecting the applicability of a particular reference system to the synchronous orbit mission sensor requirement include considerations of the reference geometry relative to the pitch, yaw, and roll control axes, intensity and vector stability of the ambient field or radiation sensed and state of development of the sensing instruments. The following sections discuss the applicability of each reference system and the associated sensors.

1.   Inertial Space Sensor Systems

The extended operating period prohibits use of gyroscopic instruments without supplementary attitude information because of inherent drift in existing designs. Integrating rate gyros may be used to intermittently furnish attitude error signals to the control system whenever the primary attitude sensor system is inoperative (for example, when the sun interferes with the proper functioning of an earth sensor). If the gyro is to be continuously operating to provide error signal upon demand, the spin motor wearout characteristics must be compatible with the three-year mission. Tests performed by Honeywell Boston Division have shown that MIG instruments with ball bearing supported spin motors are not acceptable for long duration operation. The failure rate for a group of 55 units tested a total of 600,000 hours was 30 percent in 1 year, 80 percent in 2 years, and 95 percent in 3 years of operation. Hydrodynamically (gas bearing) supported spin motors are theoretically capable of the long duration operation, since metal-to-metal contact and resultant wear are eliminated. However, experimental proof of this capability has not been demonstrated.

Through the use of a hydrostatically-supported gimbal, which eliminates jewel pivot friction, the acceleration insensitive drift rate (caused by flex lead reaction torque) may be reduced to 0.5 deg/hour maximum while random drift rates of 0.006 deg/hour are attainable. These drift rates indicate that although an integrating gyro could not maintain the attitude orientation requirements ($\pm$ 0.5 degree), they could provide control error signals for a 5-hour period while the primary sensor is inoperative and maintain attitude within the sensor 3 degree linear range. This compares to 10.8 deg/hour attitude error if no alternate attitude signal were supplied when the prime sensor was inoperative.

The use of inertial sensors is, therefore, limited to an alternate mode of obtaining attitude error signals for short intervals unless a supplementary sensor is employed to periodically correct the shift of the gyro reference frame.

2.   Ambient Field Sensor Systems

The gravitational and geomagnetic potential fields of the earth provide a reference system to obtain attitude information provided suitable sensing instruments are available and the field characteristics exhibit the required stability.

Measurement of the accelerations associated with gravity gradient torques exerted on an oblong object within the satellite may be employed to provide attitude error information relative to the gravitational vertical. Theoretical systems have been devised (Reference 2) utilizing groups of linear accelerometers which are capable of this sensing function; however, the gravity gradient at the synchronous orbit altitude is so small (3.3×10^{-10} g/ft) that suitable sensitive accelerometers are not available. The geopotential field, therefore, does not appear useful as an attitude reference system.

13

The geomagnetic field may be employed as a reference system by sensing of the local magnetic field vector direction with a modified magnetometer instrument. The geomagnetic field may be represented by the field of a short bar magnet at the center of the earth with a 11.5 degree tilt of its axis from the polar axis in the plane of 291 degrees east longitude. At the synchronous equatorial orbit altitude of 6.65 earth radii, the total field intensity is approximately 150 gammas with the vector direction inclined up to 17 degrees to the orbital plane normal (dependent on satellite longitude). Measurement of the vector direction relative to the spacecraft coordinates may be employed to provide yaw attitude information provided magnetic intensity and direction are sufficiently stable.

Although the geomagnetic field rotates with the satellite, the varying aspect of the sun and the solar wind results in distortion or compression of the field. Results of Explorer 10 and 12 satellite experiments have indicated the correlation of the magnetosphere disturbances to solar corona occurrences (Reference 3). The limited state of knowledge on the interactions of plasma with the magnetic field at the synchronous orbit altitude inhibits prediction of the field stability and, therefore, negates consideration of this reference system.

3.   Observation of Celestial Bodies

At the synchronous orbit altitude, the satellite will have an unobstructed view of all celestial objects whose angle to the ecliptic is greater than ± 32.3 degrees. The stars with a smaller angle, the sun and moon will be eclipsed by the earth at periodic intervals.

A sensor subsystem consisting of two or more star trackers could be combined with a star catalog memory, master clock and computer to track the continuously visible stars and compute the three axis error angles resolved to the pitch, yaw, and roll coordinate frame. The "navigation" stars would be selected from the stars which have high effective radiant intensity and sufficient

14

angular spacing to provide the required accuracy in resolving direction angles to the earth oriented coordinates.

While such a system is feasible, the complexity of the satellite on-board equipment is undesirable. To limit the number of star trackers would require that they be capable of tracking over wide angles. This implies mechanical servo drives and gimbals not compatible with the requirement of extended continuous operation.

Observation of a star located at or near 90 degree declination provides a suitable reference for attitude information about the yaw axis. The optical axis of a star sensor may be oriented on the satellite such that the deviation of the star line of sight from the optical axis provides the yaw attitude error directly.

Polaris, with a declination of 89.2 degrees, is suitable for such a reference source; however, its deviation from the desired orientation will cause a ± 0.8 degree yaw oscillation with each orbital period. Since this oscillation would add to the control system yaw attitude deadband excursion, the requirement for ± 0.5 degree attitude control will require programming of a synchronized bias signal to cancel the star reference oscillation. Polaris has an apparent visual magnitude of 2.1 and is classified as a F-8 spectral class star. The effective irradiance available from Polaris is dependent on the detector utilized; however, it is of sufficient intensity for photoemissive surfaces employed on available photomultiplier tubes. Discrimination of Polaris from the adjacent stars should be possible by amplitude selection, since the next brightest star within a 10 degree total field of view has a magnitude of 4.4 (approximately 0.12 of Polaris intensity).

The use of a Polaris tracker to obtain yaw attitude information provides an acceptable attitude sensor. Appropriate designs are discussed in the following section.

4.   Detection of Earth-Emitted or Reflected Radiation

The earth subtends an angle of 17.6 degrees when viewed from the synchronous orbit and exhibits changing phases completing a cycle each orbital period. In addition, the inclination of the orbital plane (equator) to the ecliptic results in an annual periodic motion of the sun through an angle (about the roll axis) of $\pm$ 23.5 degrees peak amplitude as viewed from the spacecraft. This motion causes eclipsing of the sun by the earth for a short interval (up to 1.15 hours) of each orbit for approximately 23 days before and after the earth passes the vernal and autumnal equinoxes (see Figure 3). This variation in reflected energy and interference of the sun's direct radiation limits use of the total reflected solar radiation spectral region by an earth sensor system.

The solar energy absorbed by the earth is partially reradiated at longer wavelengths, with the maximum spectral radiance at about 10 microns. This peak radiation coincides with the maximum transmissibility of the atmospheric window (8 to 12 microns as shown in Figure 4) and, therefore, original earth sensors were designed to include detection in this region of maximum radiant energy. Experience with these earth sensors and later measurements of the spectral distribution of the earth's radiation have shown that the radiant energy in the 8 to 12 micron range is highly variable with changes greater than 5 to 1 dependent on the meteorological conditions at the sensor field of view. This variation or "cold cloud" problem causes inaccuracies in the operation of sensors which depend on a relatively constant spatial distribution of radiant intensity over extended areas of the earth's surface.

A portion of the earth-emitted radiation in the far infrared is largely absorbed by the atmospheric constituents: water vapor, carbon dioxide, and ozone. These gases selectively absorb the longer wavelength radiation and reradiate at the same wavelength into space. The absorption band of water vapor (6.0 to 6.5 microns)

16
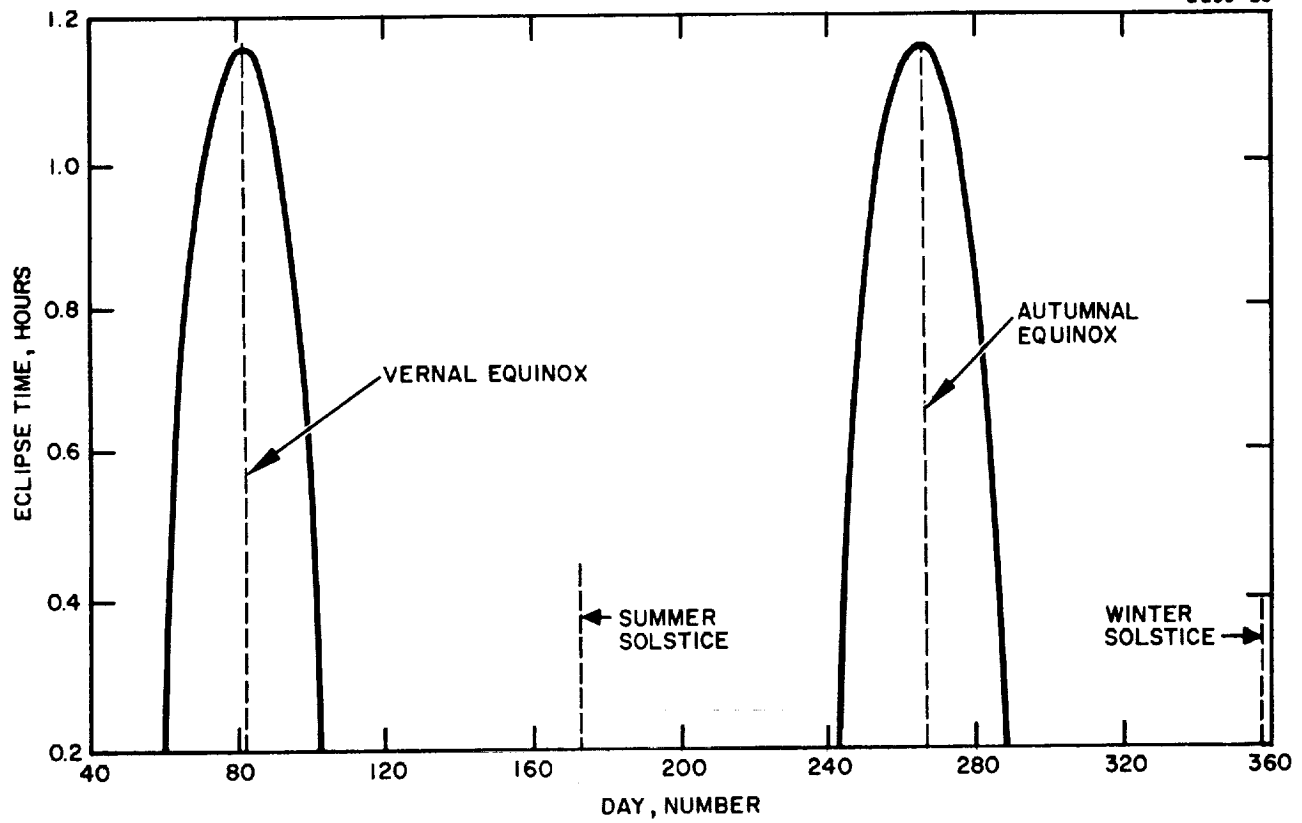
Fig. 3. Eclipsing periods of the sun.

and ozone (9.6 microns) are less interesting than the absorption band of carbon dioxide (15 microns) as shown in Figure 5. The carbon dioxide gas is uniformly distributed throughout the stratosphere and, therefore, provides a uniform spatial distribution of radiation at its emission wavelengths (14 to 16 microns).

Since narrow bandpass filters with high transmissibility are not generally available, the use of the narrow carbon dioxide spectral region is prohibited; however, extension of the bandpass from 13 to 20 microns (or higher) provides a practical sensor design and will limit detected intensity variations to less than 2 to 1.

The earth sensor operating with suitable detectors is, therefore, applicable to the determination of pitch and roll attitude errors. Earth sensors will be subject to interference from the sun and moon, since both are periodically eclipsed by the earth and, therefore, may enter the sensor field of view. Since the sun has approximately 100 times the earth's intensity in the spectral region of interest, the interference of the sun will produce false error signals. The radiant energy from the moon will produce similar errors. Applicable earth sensor designs are discussed in the following section.
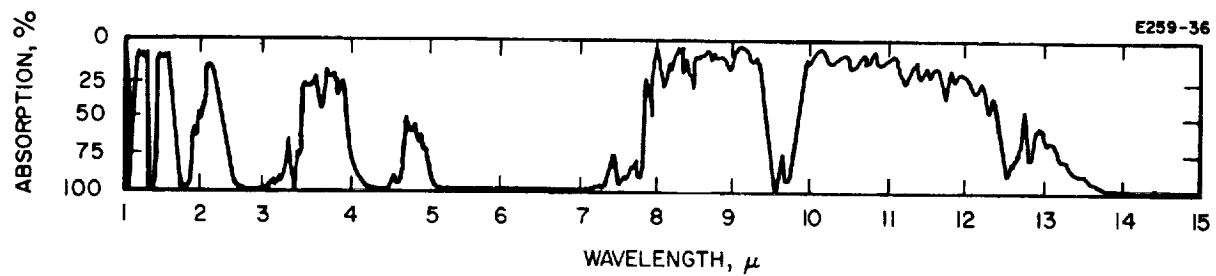
Fig. 4. Spectral absorption of the atmosphere.
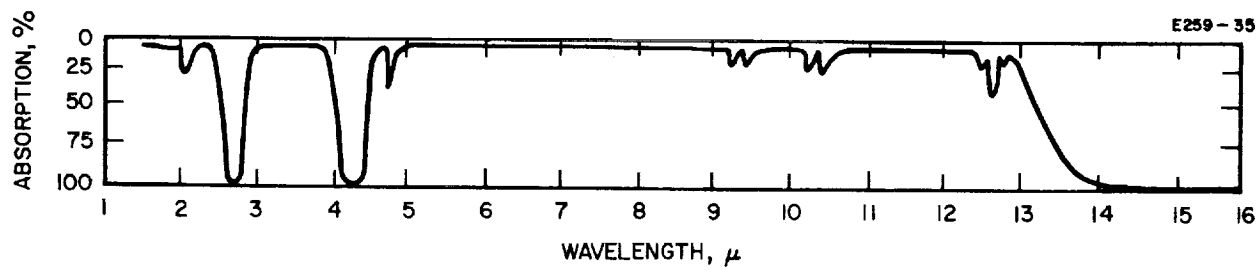
Fig. 5. Spectral absorption of carbon dioxide.

19

C.   DESCRIPTION OF APPLICABLE SENSOR SYSTEMS

The prime candidates for attitude sensors to satisfy the mission requirements and system constraints are star sensors to determine yaw attitude by reference to the line-of-sight to Polaris, and earth sensors to obtain attitude information about the pitch and roll axes. A survey of available star and earth sensor designs has been performed and several proposed designs have been evaluated.

The following paragraphs describe the sensor designs and evaluate their suitability for this application.

1.   Star Sensor Systems

Design of a star sensor requires definition of the total field of view required for the mission to determine discrimination techniques that may be employed. Although the $\pm$ 3 degree linear range required of the sensor (Table I) defines the maximum field of view necessary, it has been arbitrarily extended to $\pm$ 5 degrees to investigate discrimination problems. The star field within the region of Polaris is presented in Figure 6 for declinations greater than 70 degrees. Stars are identified by name, visual magnitude number, and special classification. This star map shows that the next brightest star in the region of interest is Ursa Minor, which is 0.12 times Polaris intensity. Available photodetectors will discriminate this intensity difference; therefore, amplitude selection may be used for identification of Polaris in the sensor field of view.

Available star sensor designs consist of a refractive or reflective optical system with the aperture diameter selected to intercept sufficient star radiation to provide the required signal-to-noise ratio. The optical axis defines the reference axis and angular deviation of the line of sight from this axis may be resolved (by electronic processing) into two orthogonal planes which provide two axis attitude information. Since the ion engine control system requires only single axis attitude error information from the star

20
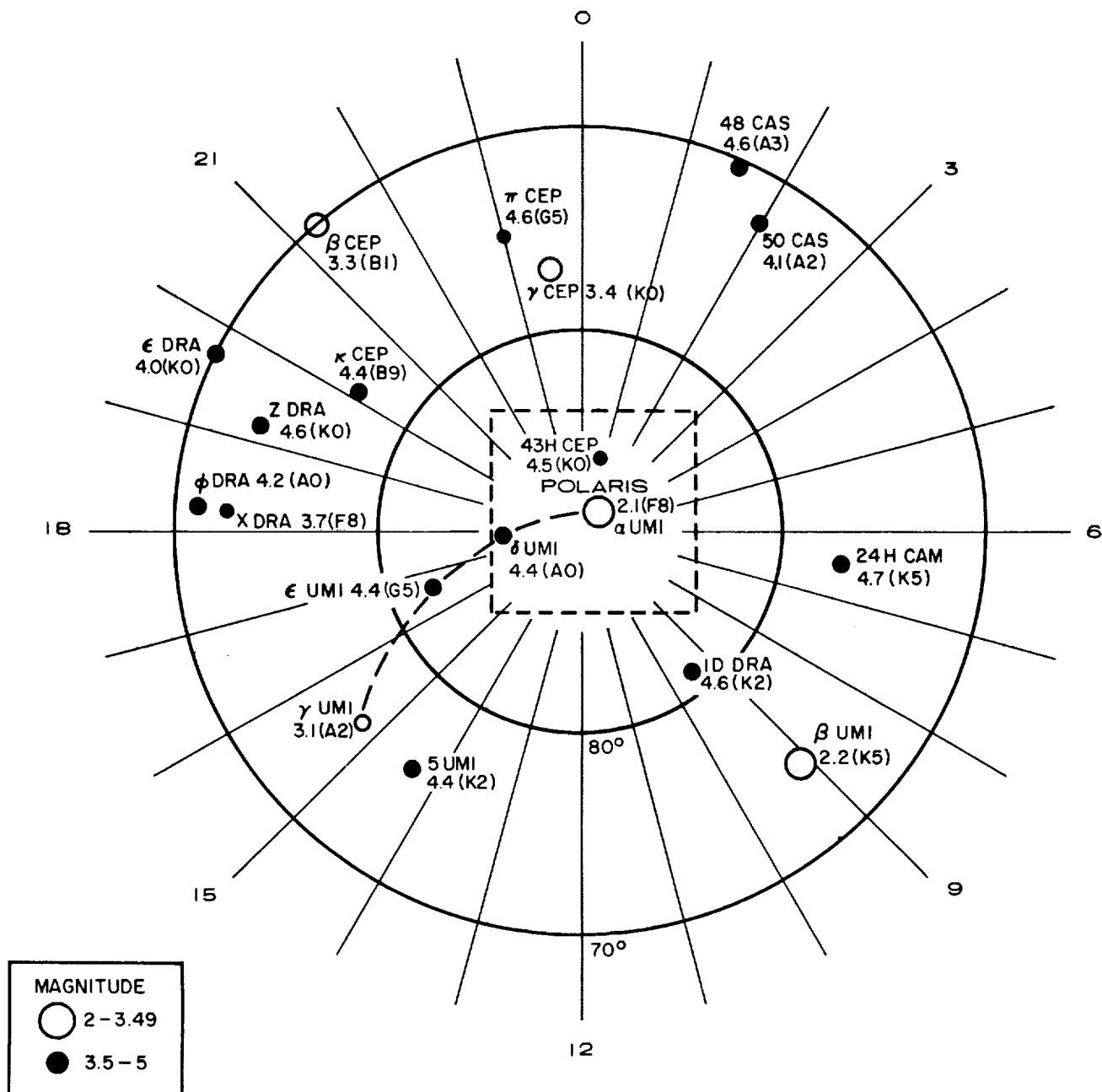
Fig. 6. Star field in the region of Polaris.

tracker (about the yaw axis), the line of sight angle would be resolved into a plane perpendicular to the yaw axis.

The sensor total field of view is scanned either mechanically by an oscillating optical element prior to focusing of the star on a photomultiplier detector or it is scanned electronically after focusing of the field of view on an image dissector tube.

The mechanically scanning star tracker design, such as the Canopus sensor employed on the Surveyor spacecraft (Reference 4), is not suitable for this application since the wearout characteristics of the scanning mechanism would limit operational life. Although mechanical scanning may be obtained using non-wearing flexure pivots, the electronically scanned sensor design appears to offer greater ability for long term operation with less complexity. Further discussion is, therefore, limited to the latter design.

The image dissector tube consists of a photocathode, electron lens system, aperture plate and an electron multiplier section packaged in a glass envelope. Two variations of the tube are shown schematically in Figure 7.

The photocathode element converts the optical image focused on the tube window to an electron image which is electrostatically focused and accelerated toward the aperture plate. The tube window, which serves as the photocathode supporting substrate, is made of lime glass or Kovar-sealed borosilicate glass. The photoemissive surface (antimony-cesium-sodium-potasium materials) is deposited on an intermediate layer of semitransparent, electrically conductive material. Tubes are designated by S-numbers according to their spectral response which includes the transmission of the window. For the F-8 spectral distribution of Polaris (approximately a 6000° K black body source), tubes designated as S-20 provide the best available characteristics. Spectral response of typical S-4, S-11, and S-20 detector tubes are shown in Figure 8.

OPTICAL AXIS

PHOTO CATHODE

*IMAGE
DISSECTION
SECTION*

ELECTROSTATIC LENS

APERTURE
PLATE

Ⓐ

Ⓑ

Ⓐ

Ⓑ

①

*ELECTRON
MULTIPLIER
SECTION*

②

④

③

⑤

⑥

⑦

⑧

⑨

⑩

⑪

⑫

⑬

⑭

⑮

⑯

Ⓘ

VACUUM TUBE
ENVELOPE

Ⓒ

**(b) CONTINUOUS CHANNEL
PHOTOMULTIPLIER**

Ⓒ

**(a) MULTIPLE DYNODE
PHOTOMULTIPLIER**
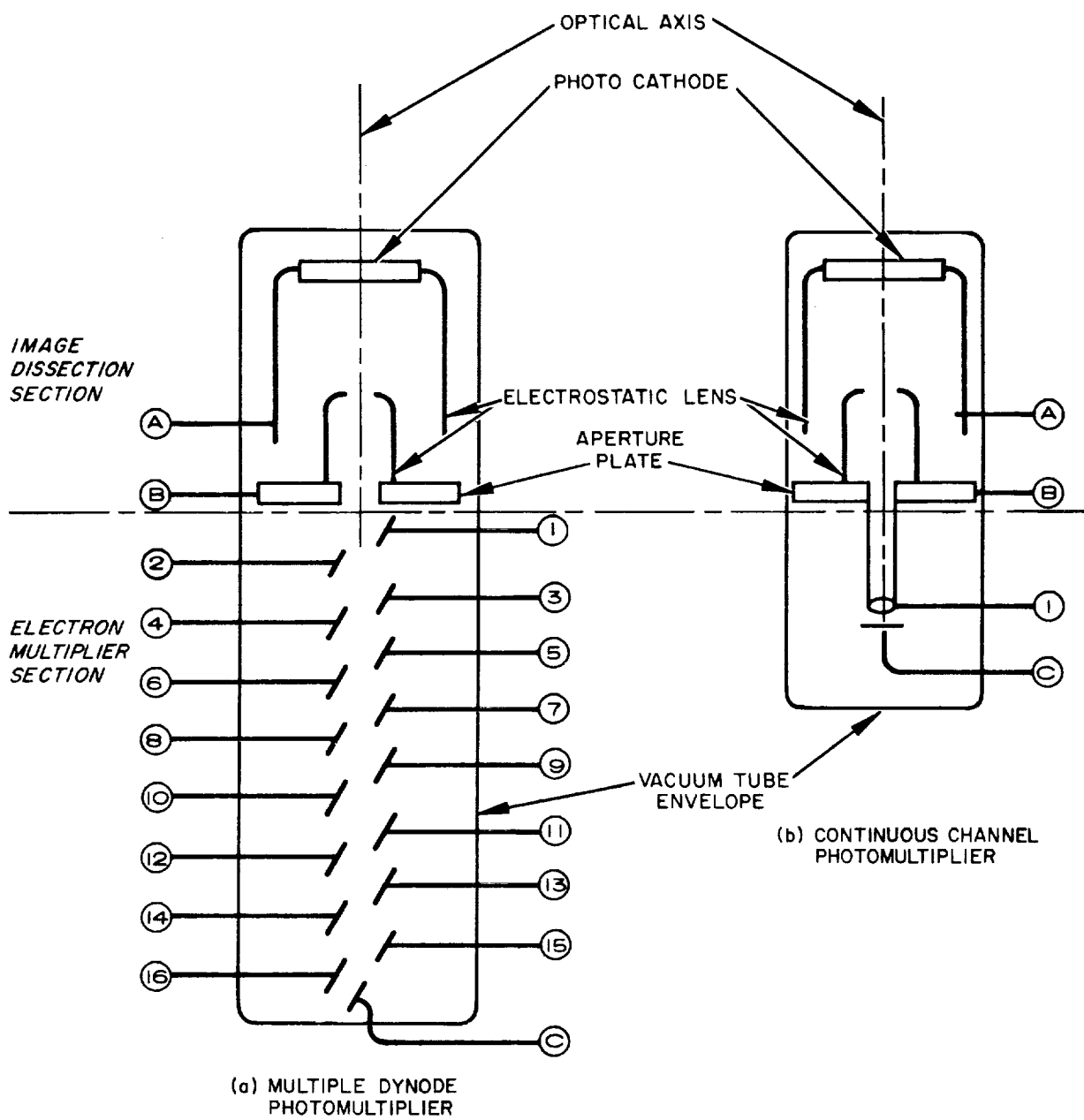
Fig. 7. Image dissector tube schematics.
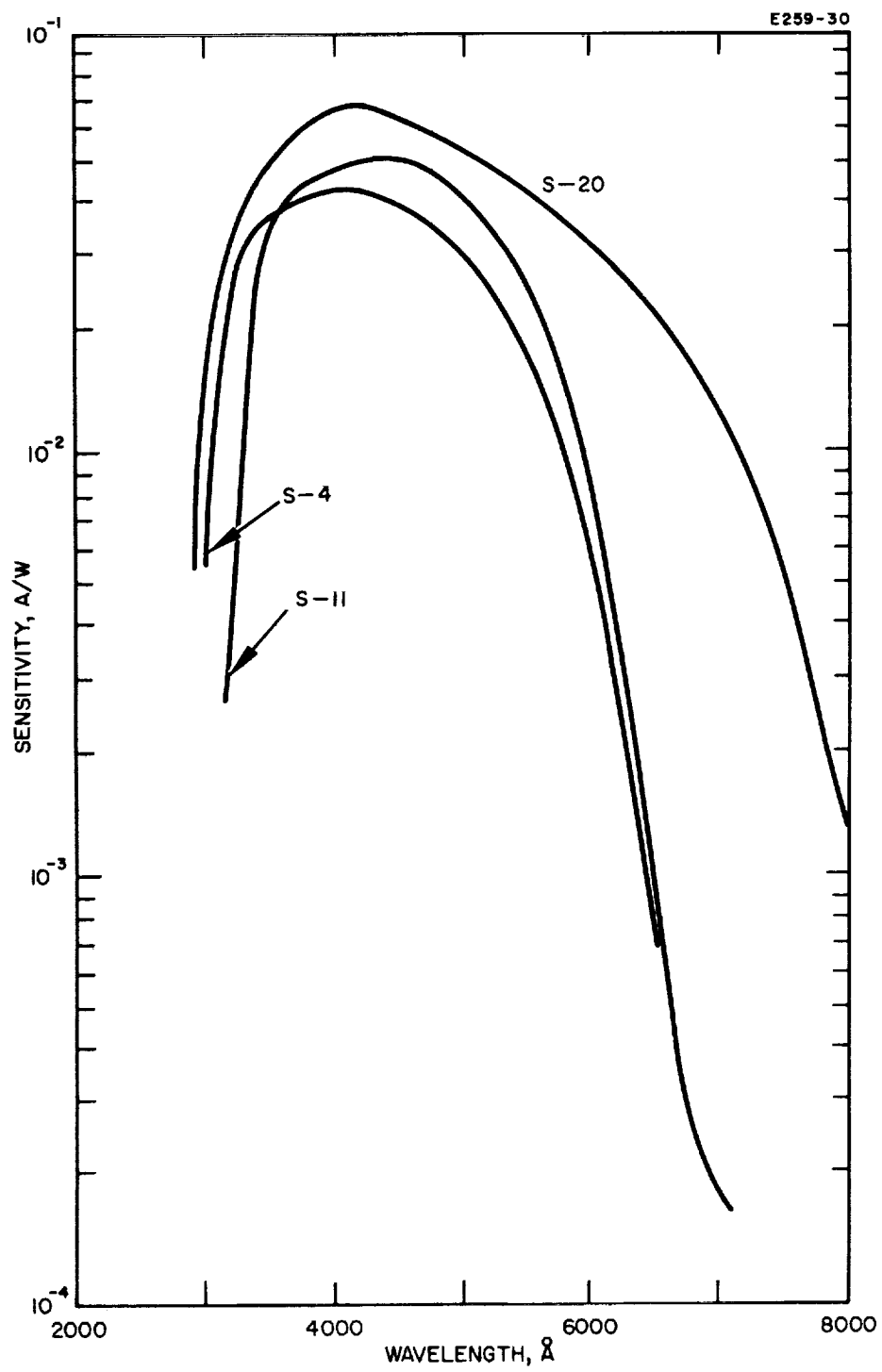
Fig. 8. Image dissector tube spectral response.

24

To provide a scanning of the sensor total field of view so that the angular position of Polaris is detected, external electrostatic plates or Helmholtz coils are employed to sweep the electron image across the aperture. Thus, when the electron image of Polaris is focused on the aperture, the multiplier section provides a signal output at the collector electrode which, when compared with a sweep signal reference, gives angular position of the star relative to the telescope boresight.

The electron multiplier section which amplifies the star signal may take the form of a multielement dynode construction or a continuous channel. In the dynode multiplier, the incident electron entering the aperture impinges upon the first dynode (a metal plate with a secondary emission magnesium oxide film). The secondary electrons produced are accelerated axially toward the second dynode by a progressively increasing potential of the dynodes. Electrons striking the second dynode also cause secondary emission and the electron amplification continues down the cascaded elements to the collector.

The continuous channel electron multiplier is made of a hollow glass tube (0.03" typical diameter) with a deposited high resistivity inner surface. A high potential (2000 volts) is connected across the tube ends so that a uniform potential field is established down the length of the tube. The incident electron entering the aperture impinges on the side of the tube causing emission of secondary electrons which have a transverse velocity and are accelerated parallel to the tube axis by the electric field. These electrons, in turn, strike the tube wall releasing more electrons and the process continues the length of the tube to the collector electrode as shown in Figure 9.

The channel multiplier has the advantage of less mechanical complexity as compared to the dynode multiplier. However, the noise figure for this design increases with increasing gain, whereas the dynode design noise figure approaches a constant value as gain is increased.

$\bar{\theta}$

ℓ

END VIEW

ENLARGED VIEW OF
ELECTRON TRAJECTORY
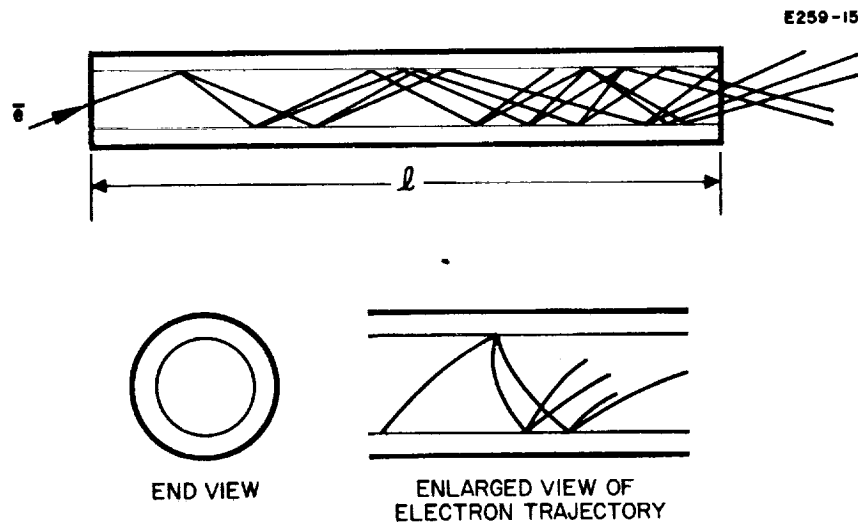
Fig. 9. Continuous channel electron multiplier.

The signal received at the collector electrode is electronically processed to discriminate between Polaris and other stars and to convert the information into an analogue output signal proportional to attitude error angle.

Polaris Radiant Intensity

Star irradiance must be converted to effective irradiance for the relative spectral response of the detector employed. Limited stellar spectral data is available since astronomical measurements on star color are usually given in terms of irradiance measured through ultraviolet, blue, or yellow-green filters. Santa Barbara Research Center has analyzed such data and devised a computation program to determine effective spectral magnitude for any photodetector response (Reference 5).

Following this method of computation, the total effective irradiance H (m) for Polaris may be computed by

$$H\ (m)\ =\ \int_{\lambda_1}^{\lambda_2} H\ (\lambda)\ R\ (\lambda)\ d\lambda \qquad (watts/cm^2)$$

where

$H\ (\lambda)$	=	spectral irradiance measured outside the earth's atmosphere $(watts/cm^2/micron$, computed from star color data)
$R\ (\lambda)$	=	relative spectral response of the photocathode
λ_2	=	upper cutoff of detector (microns)
λ_1	=	lower cutoff of detector (microns)

The total S-20 effective irradiance for Polaris is approximately 1.3×10^{-13} watts/cm^2 using this method of computation.

Adequacy of Polaris Effective Radiant Intensity

The signal output (I_s) at the collector electrode of the image dissector tube is given by

$$I_s = P_c \, R_c \, G \qquad \text{(amperes)}$$

where

P_c = effective radiant flux on the cathode (watts)

R_c = peak photocathode responsivity (amp/watt)

G = the gain of the multiplier tube

The effective radiant flux is given by

$$P_c = H(m) \, \frac{\pi}{4} \, D^2 \, t \qquad \text{(watts)}$$

where

D = optical aperture diameter (cm)

t = optical system transmissivity

For practical values of the design parameters, signal currents in the order of 10^{-7} amperes are obtainable which will be suitable for the video preamplifier operation.

Signal-to-Noise Relationship

All photoemissive dissector tubes are photon shot noise limited; therefore, the RMS noise (I_n) is given by

$$I_n = [2 \, e \, I_a \, \Delta f]^{1/2} \qquad \text{(ampere)}$$

where

e = the electron charge (1.6×10^{-19} coulombs)

Δf = the electronic bandwidth of the video amplifier (cps)

I_a = the aperture current (I_s/G) (amperes)

The signal-to-RMS noise ratio (N_r) is, therefore,

$$N_r = \left[\frac{I_a}{2 \, e \, \Delta f} \right]^{1/2}$$

Description of Candidate Polaris Star Sensors

Proposals have been received from four companies for star sensor designs utilizing image dissector tubes. The designs differ mainly in the optical design, raster scan method, and the electronic signal processing system. All of the available image dissector tubes are used by the various candidate systems. Table II presents a summary of the characteristics of the proposed designs.

Bendix Corp. Star Sensor Design

The Polaris sensor proposed by Bendix Corp. (Reference 6) utilizes refractive optics, the Bendix Channeltron image dissector tube with two axis electromagnetic scanning, and digital electronics signal processing to obtain the attitude error signal. A functional block diagram of the sensor is shown in Figure 10.

The x-axis sweep is made in a plane normal to the yaw axis; therefore, the angular displacement of the sweep when Polaris is detected is the desired attitude error information. The y-axis sweep frequency is fixed at 10 cps so that the entire photocathode surface is scanned every 0.1 second, consistent with the maximum specified time constant. The x-axis sweep serves a dual purpose in deflecting the photocathode electron stream and providing a synchronizing signal to the signal processing electronics. The relationship between the x-axis sweep voltage and the photocathode scan is shown in Figure 11 (a) when no star is detected and in Figure 11 (b) when a star is detected on the line of scan.

To obtain the star location, the positive going voltage at the end of the blanking pulse enables a gate in the digital control logic which passes pulses from the master oscillator into a binary register. The gate is inhibited whenever a star signal exceeding a threshold value is detected on a line scan, or if no star is detected, when the negative going voltage at the end of the sweep occurs. If no star is detected, the register is reset to zero. The pulse count in the register is, therefore, proportional to the position of the star.

TABLE II

CANDIDATE POLARIS STAR SENSOR DESIGN CHARACTERISTICS

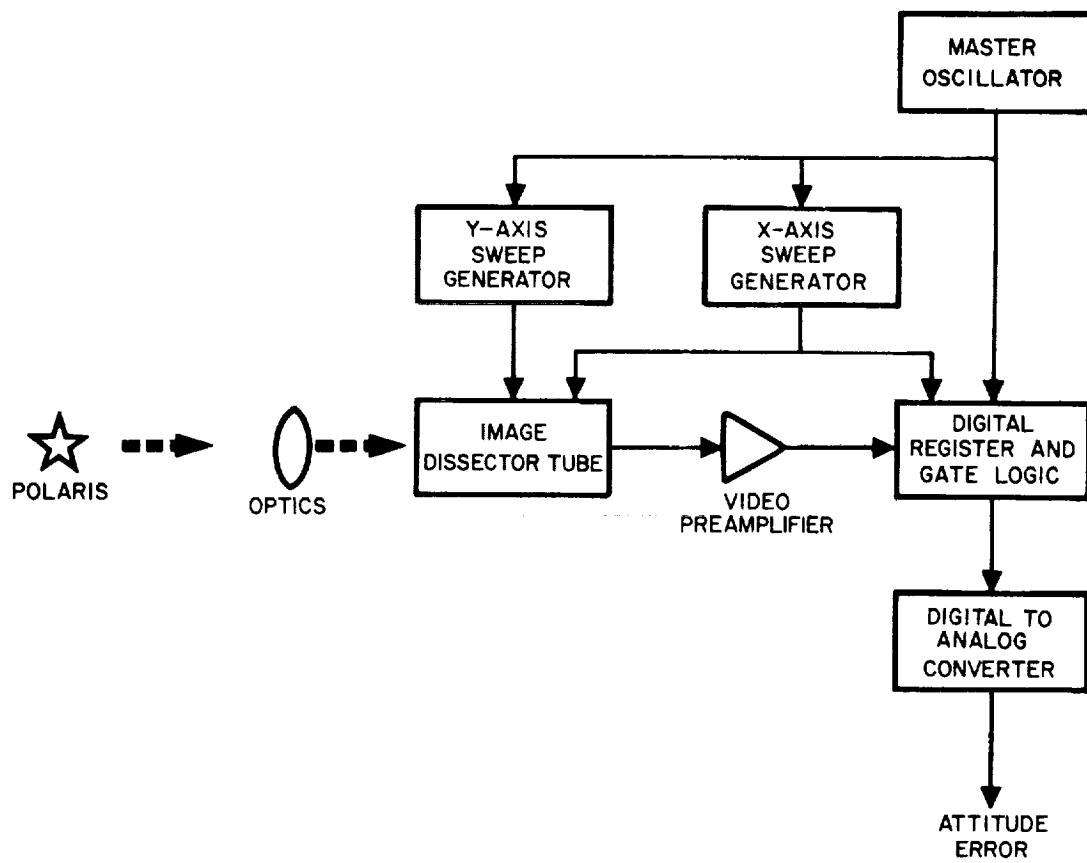| CHARACTERISTIC	BENDIX	ITT	SBRC	BARNES
1. Optical System				
Aperture Diameter (in.)	2.05	2.09	2.45	1.00
Focal Length (in)	3.07	1.77	2.45	0.80
f/ Number	f/1.5	f/0.85	f/1	f/0.8
Transmissivity	-	0.5	0.7	-
Total field of view (deg)	10x10 rect.	9.9 circular	10.5 circular	4x10 rect.
Instantaneous field of view (deg)	circular	1x10 rect.	1x10.5 rect.	0.86x10.6 rect.
2. Detector				
Image dissector tube	Bendix Channeltron	ITT FW-143	CBSCL-1147	CBSCL-1147
Cathode spectral classification	S-11	S-20	S-20	S-20
Peak cathode response (amp/watt)	0.05	0.064	0.064	0.064
Wavelength of peak response (micron)	0.44	0.42	0.42	0.42
Useful cathode dia. (in)	0.75	0.3	0.5	0.5
Aperture size (in)	small dia. hole	rect.	0.005x0.45 rect.	0.010x0.125 rect.
Type of electron multiplier	channel	Dynode	Dynode	Dynode
Type of sweep deflection	electromagnetic	electromagnetic	electrostatic	electro-static
3. Signal Processing				
Scan Rate (cps) Horizontal	300	250	65	1000
Vertical	10	none	none	none
Amplifier Bandwidth (cps)	30000	3000	2400	-
Output noise (mv)(estimated)	8	24	6	12
4. Physical Package				
Outline Dimensions (in)	4.0x7.0x10.0	2.25diax8.5 L.	3.5diax9.5 L.	4.5x5.0x11
Weight (pounds)	5	8	-	6
Power (watts)	8	-	-	3.5

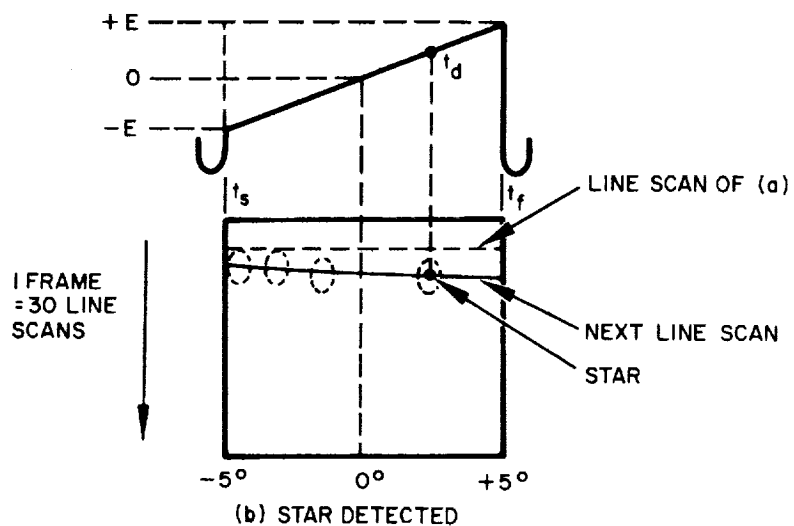Fig. 10. Bendix sensor functional block diagram.

31
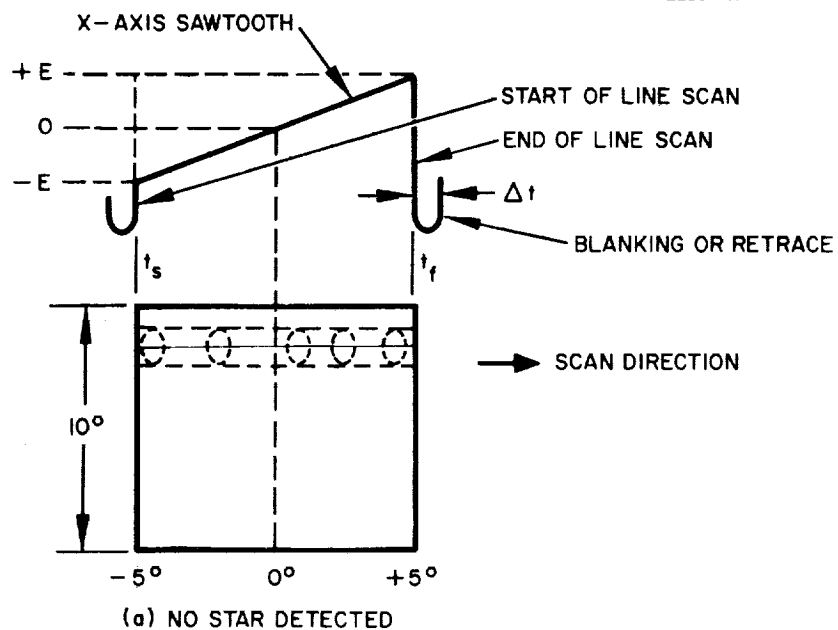
Fig. 11. Sweep voltage and photocathode scan relationship.

The detected star clears the binary memory of a digital-to-analog converter and then transfers the binary count of the register to the memory. If no star is detected on a single line scan, the DAC memory remains in the previous state and the analog output remains unchanged.

The limiting accuracy of the signal processing is the number of pulses produced during a single line scan or the granularity of one scan cycle. To obtain the required 0.1 degree accuracy in the 10 degree total field of view, 100 pulses must be available from the master oscillator during a single scan. The oscillator frequency (f) is, therefore,

$$f = \frac{100}{\tau - \Delta t} \qquad \text{(pulses/sec.)}$$

where

τ = scan period (sec)

Δt = blanking pulse duration (sec)

For the scan rate of 300 cps, an oscillator frequency of approximately 31,000 cps will be required. The binary digital registers have a scale (total count) of 128 to insure sufficient granularity. Stability of the master oscillator is maintained to 0.17 percent and the sweep circuit oscillator stabilities are better than 0.5 percent. Accuracy of the digital-to-analog conversion is held to within 0.25 percent.

Bendix has designed and fabricated a star tracker for use in the OAO satellite control system. This sensor utilizes the ITT Federal Laboratories image dissector tube as the detector. The telescope and detector are mounted on a two degree of freedom servopositioned gimbal system. A star sensor has not been developed using the channeltron image dissector tube and ability of the tube to provide sufficient signal from Polaris is questionable.

The sensor design has been constrained by the noise characteristics of the channel electron multiplier (increasing noise with

increasing gain) which evidently holds the practical gain to 10^5 versus 10^7 for the dynode multipliers. This lower gain forces the design into a two axis sweep to reduce the scanning spot area, thereby reducing background noise. The wide bandwidth (30 KC) video amplifier design also becomes necessary to obtain adequate signal-to-noise ratios.

ITT Federal Laboratories Star Sensor Design

The ITT Federal Laboratories has proposed a Polaris tracker utilizing the ITT image dissector tube with an objective lens to focus the 10 x 10 degree total field of view on the photocathode (Reference 7). The electron image on the photocathode is scanned 250 times per second with a 1 x 10 degree instantaneous field of view through a 12 degree total scan sweep angle. A star image on the photocathode, therefore, provides a square wave pulse output with a duration of 1/12 scan period. The position of the star in the field of view determines the position of this pulse relative to the sweep sawtooth voltage waveform.

The functional block diagram for the sensor is shown in Figure 12. A free running multivibrator is employed as a master oscillator to supply signals for the sweep generator and gating functions. At the start of a sweep, a gating pulse switches a bi-stable multivibrator so that its output stage is conducting. The square wave star signal pulse from the video amplifier switches the bistable multivibrator off; therefore, the width or duration of the multivibrator output is a linear function of the star's position. This output is filtered to obtain the linear d.c. attitude error signal. Voltage levels of the bistable multivibrator are designed so that a zero output voltage is obtained with the star on the optical axis.

The video amplifier contains automatic threshold circuitry to reject all photomultiplier signals less than half the peak amplitude of the largest signal present (Polaris). The threshold level is adjusted to discriminate as near the peak signal as possible while providing sufficient signal for operation.

34

E259-28

SWEEP GENERATOR

INVERTER

GATE

∫

∫

Σ

SIGNAL PROCESSING
CIRCUITS

ERROR
SIGNAL

FILTER

BSMV

AMPLIFIER

PHOTO
MULTIPLIER
TUBE

ASMV

DIVIDER
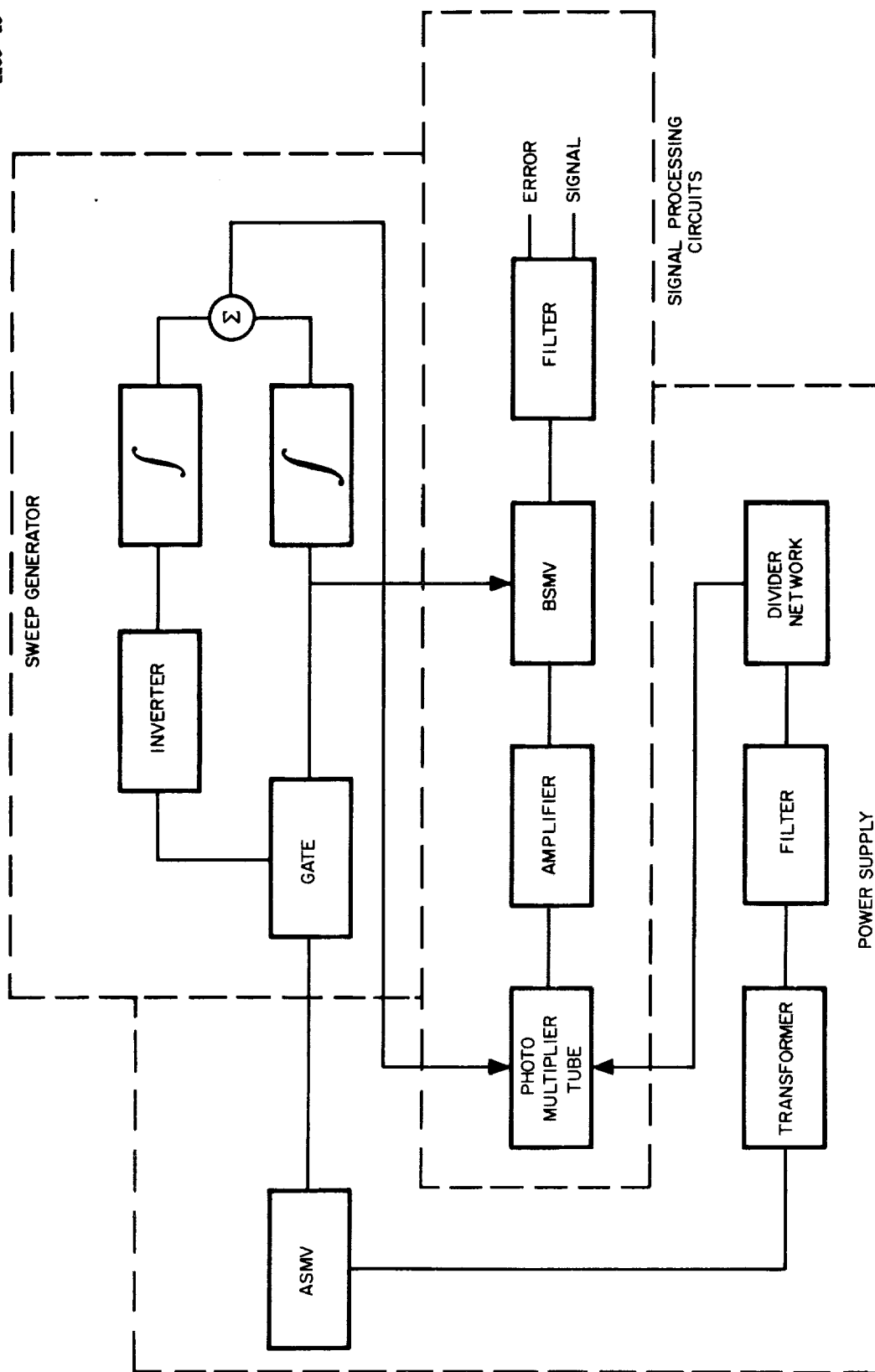NETWORK

FILTER

TRANSFORMER

POWER SUPPLY

Fig. 12. ITT sensor functional block diagram.

35

Sensor accuracy is dependent on the stability of the sweep, bistable multivibrator switching delays and output amplitude stability, output filter stability, and consistency of the video amplifier pulse shape. The first three conditions may be controlled to provide negligible error through proper circuit design. The video pulse shape is affected by the noise distortion of the pulse; therefore, the bistable multivibrator switching time is dependent on noise superimposed on the video signal. There is, however, an average switching time which, when taken over a large number of samples, provides a consistent error signal. If the video pulse leading edge is nonlinear, the average switching time will not coincide with the time at which the signal attains the switching level; if the pulse leading edge is consistent, the average is constant and can be calibrated to contribute a minimum error to the system.

The limit on sensor accuracy is, therefore, established by the random nature of the time at which the video pulse reaches the bistable multivibrator switching level. Approximating the pulse as a half-sine wave gives the rms value of this time variation (when averaged over one filter time constant) as 8.06×10^{-6} seconds, which is equivalent to a sensor output signal error of ± 0.012 degrees. The sensor design, therefore, appears capable of meeting the accuracy requirements of this application.

Barnes Engineering Co. Sensor Design

The Polaris star sensor proposed by Barnes Engineering Company is based on the Canopus sensor jointly developed with Jet Propulsion Laboratory for the Mariner C spacecraft. The Polaris sensor design employs the CBS image dissector tube with refractive optics providing a 4 x 10.6 degree total field of view. This design may be modified to 10 x 10 degree field of view; however, a minimum modification of the Mariner C sensor design is proposed.

The functional block diagram for the sensor is shown in Figure 13 and the relationship between the video output pulses and the photocathode scan for various star locations is shown in Figure 14. The scanning of the photocathode is made with a 1000 cps sinusoidal sweep voltage so that the time occurrence of the video output pulses depends on the location of the star in the field of view. The instantaneous field of view defined by the aperture at the photomultiplier is 0.86 degree by 10.6 degrees. Only stars above a preset threshold discrimination level within the total field of view provide the series of output pulses. This level is set so that Polaris will provide the only video pulses.

The series of video pulses are introduced into a 1000 cps filter of 50 cps total bandwidth (-6 db points) and the output of the filter is, therefore, a 1000 cps signal, the magnitude of which is proportional to the angular location of the star. (This can be shown by Fourier analysis of the pulse train.) The phase of the output signal is 0 or 180 degrees, depending on the polarity of the star's position. This signal is phase detected, demodulated and amplified to provide the linear d.c. attitude error signals.

The Mariner sensor, similar to this design, has functioned properly while tracking a + 4.2 magnitude simulated star or approximately 0.15 times Polaris intensity. A quantity of 10 units are presently being fabricated for the Mariner program. Modification of the unit to the larger total field of view desired will require changes in the optical system and the sweep deflection generator. Output noise level of the sensor has been measured at 50 millivolts for an 8 volt/degree scale factor; however, frequency spectrum of the noise has not been determined.

Santa Barbara Research Center Star Sensor Design

SBRC has proposed a Polaris sensor design with refractive optics also utilizing the CBS image dissector tube (Reference 8).
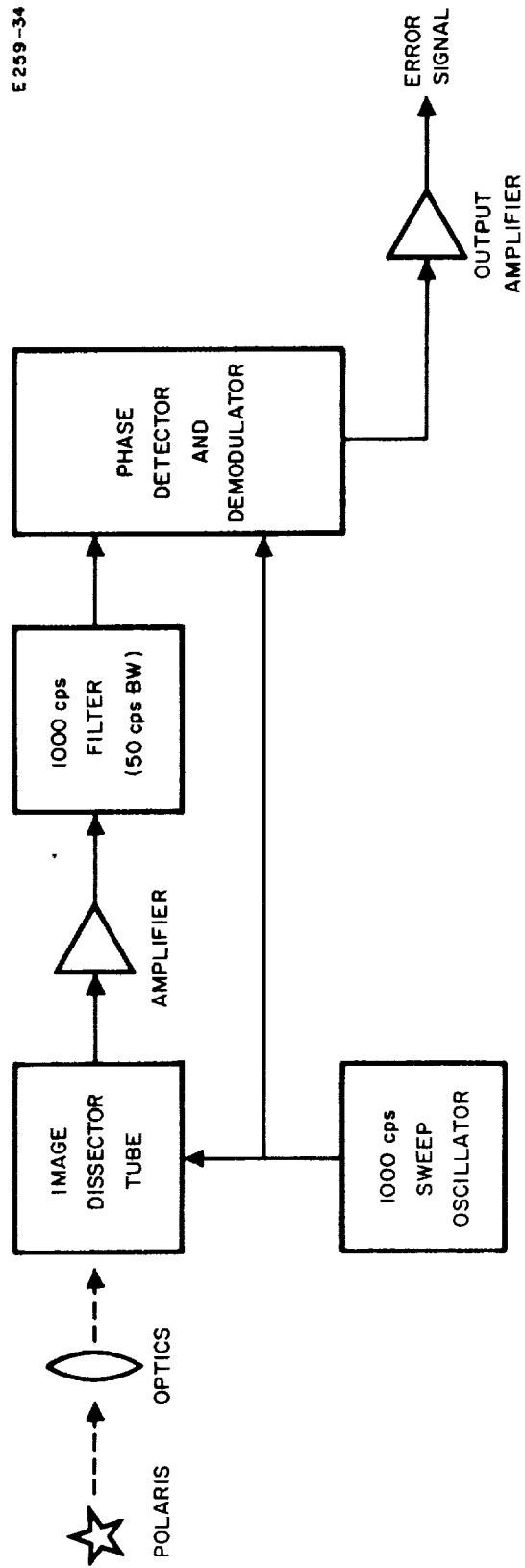
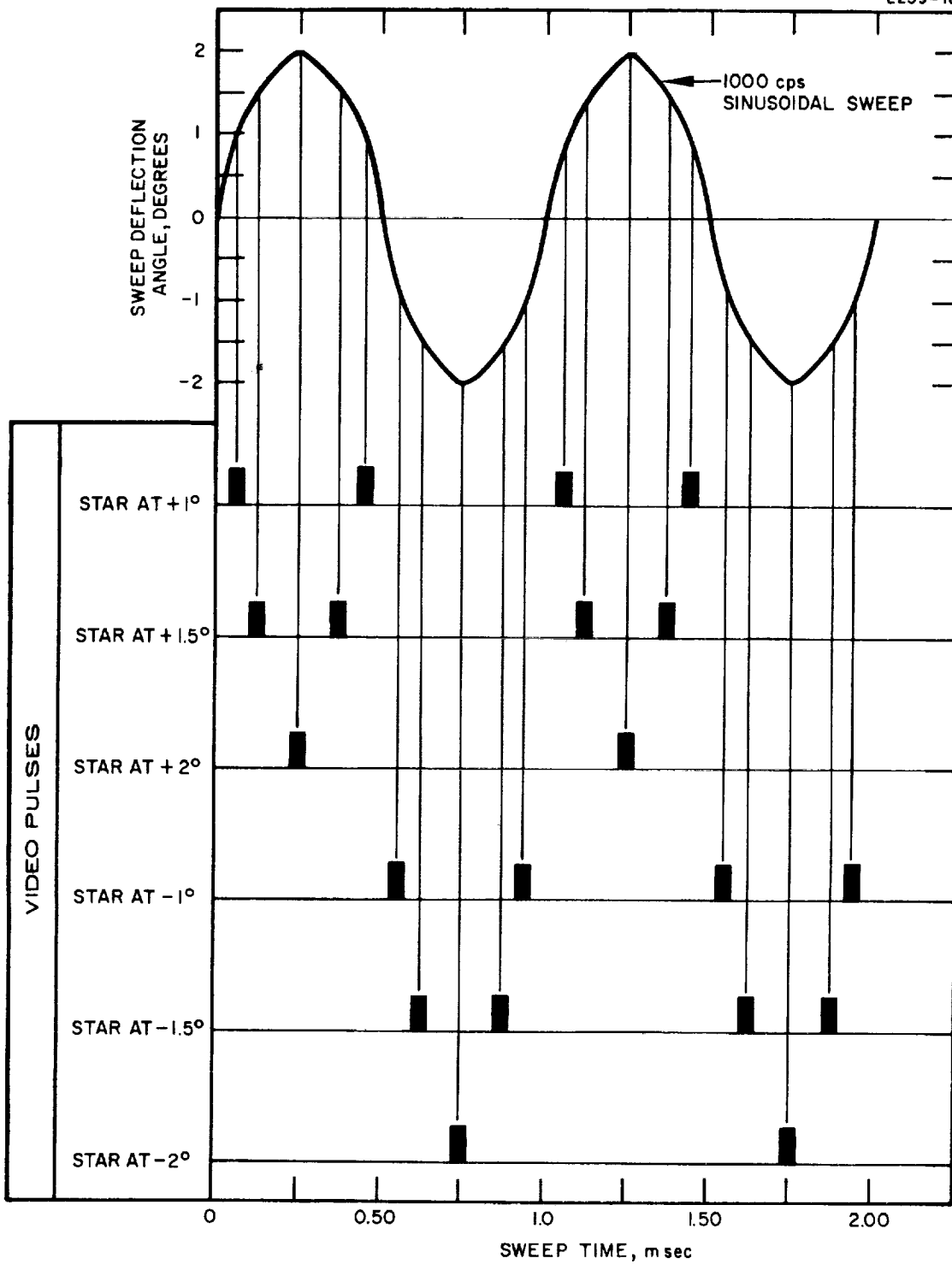Fig. 13. Barnes sensor functional block diagram.

Fig. 14. Video signal and photocathode scan relationship.

The telescope images a 10.5 degree diameter total field of view on the window of the image tube. This image is electronically scanned at a 65 cps rate and the video pulses obtained during a scan are time correlated with the sweep deflection voltage to obtain the star location in the field of view. The functional block diagram for this sensor is shown in Figure 15; the scanning geometry is illustrated in Figure 16.

The amplified video pulse caused by Polaris in the field of view is discriminated by threshold level circuitry (clipped and limited; see signal waveforms of Figure 17).* The output pulses of the limiter-clipper are used to gate a reference ramp voltage which is synchronized to the scanning sweep. The gated reference signal is peak detected and filtered to obtain the d.c. output error signals.

To provide for long term stability of the sensor null position, a continuous calibration system is designed into the sensor. This system places a small spot of light at the null position of the tube (by the use of small lamps and fiber optics) on every tenth scan of the image so that scan calibration data is obtained to reposition the scan centering voltage. A blanking gate preceding the limiter-clipper is utilized to prevent the calibrate scan signal from entering the video process circuitry.

An AGC system which regulates on the Polaris video signal is also provided to compensate for aging of the amplifier and power supplies associated with the image dissector tube.

The limiting accuracy of the sensor will be determined by the time jitter of the gated reference voltage pulse, which is determined by the variation of the video pulse shape with superimposed noise. This variation can be controlled to provide the required 0.1 degree sensor accuracy by straightforward circuit design techniques.

SBRC has developed the Canopus star tracker (mechanically scanned) utilized on the Surveyor spacecraft and has, thereby, developed a background in star tracker design techniques including signal

40
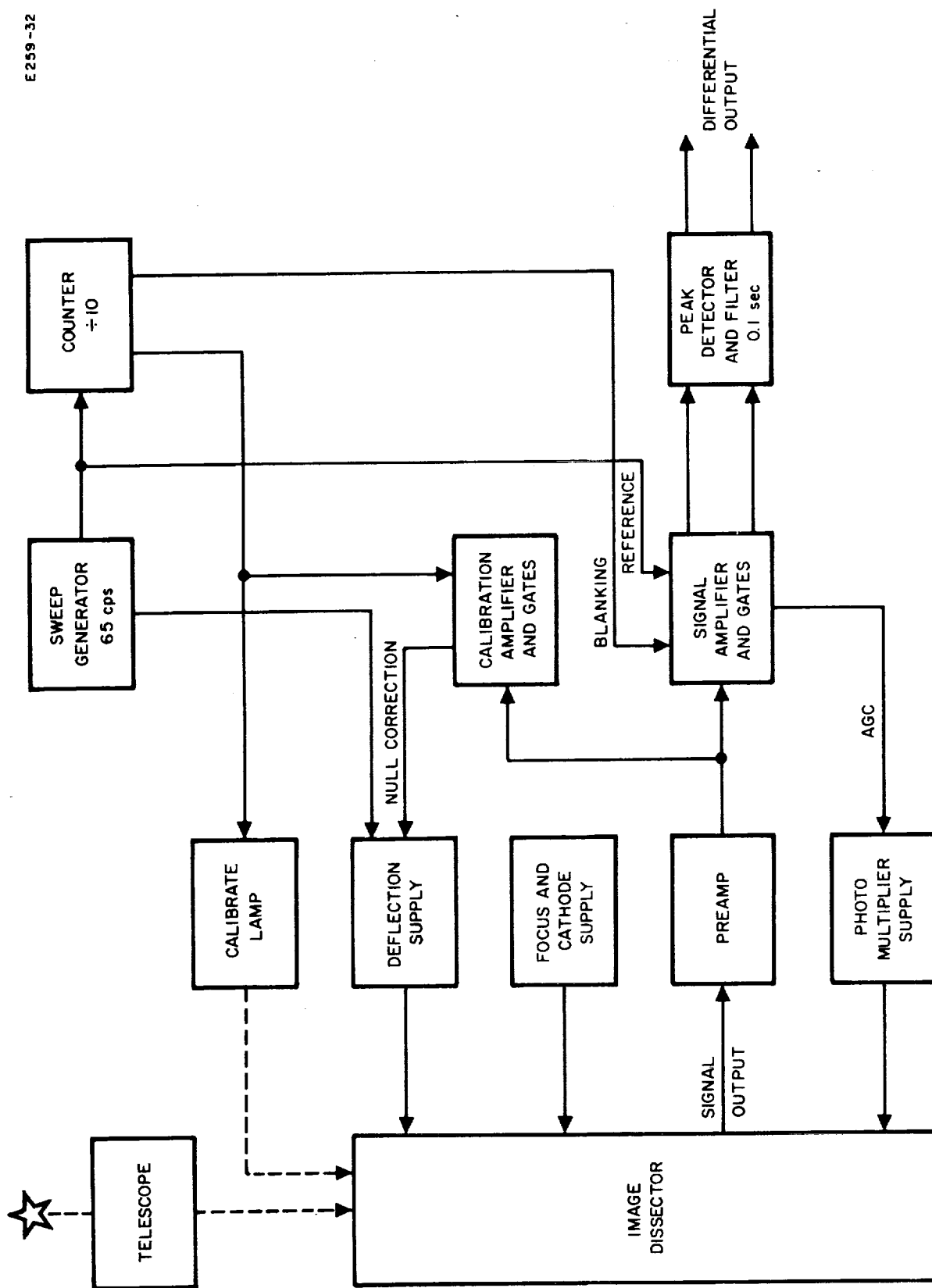
Fig. 15. SBRC sensor functional block diagram.

FIELD STOP

TUBE FACE

INSTANTANEOUS
ELECTRONIC FIELD
OF VIEW

10.5°

SCAN LIMITS

REFERENCE INPUT LOCATION

Fig. 16. Sensor scanning geometry.

RAW VIDEO SIGNAL

CLIPPED AND LIMITED

REFERENCE

GATED REFERENCE

PEAK DETECTED

Fig. 17. Signal processing waveforms.

processing of the video star pulse signal and problems associated with star signal discrimination.

The SBRC Sensor design as well as the Barnes and ITTFL designs employ a narrow rectangular instantaneous field of view (approximately 1 x 10 degrees). The video signals of these sensors at any instant in the scan will be a pulse with magnitude proportional to the sum of all light sources within the instantaneous field of view. The possibility exists that several dimmer stars within the 10 x 10 degree total field of view may be summed to give a false signal which will exceed the threshold level. SBRC has investigated this possibility and found three stars (43 H. Cep., δ U. Mi. and ε U. Mi.) which roughly form a straight line (i.e., within the 1 x 10 degree field). The effective radiant intensity of this group has been calculated and found to be 0.4 times Polaris intensity and, therefore, magnitude discrimination is not compromised.

General Discussion of Proposed Designs

The use of the channel type electron multiplier in the Bendix sensor design produces added circuit complexity (i.e., dual channel sweep) over the sensors utilizing the dynode type multiplier. This additional circuit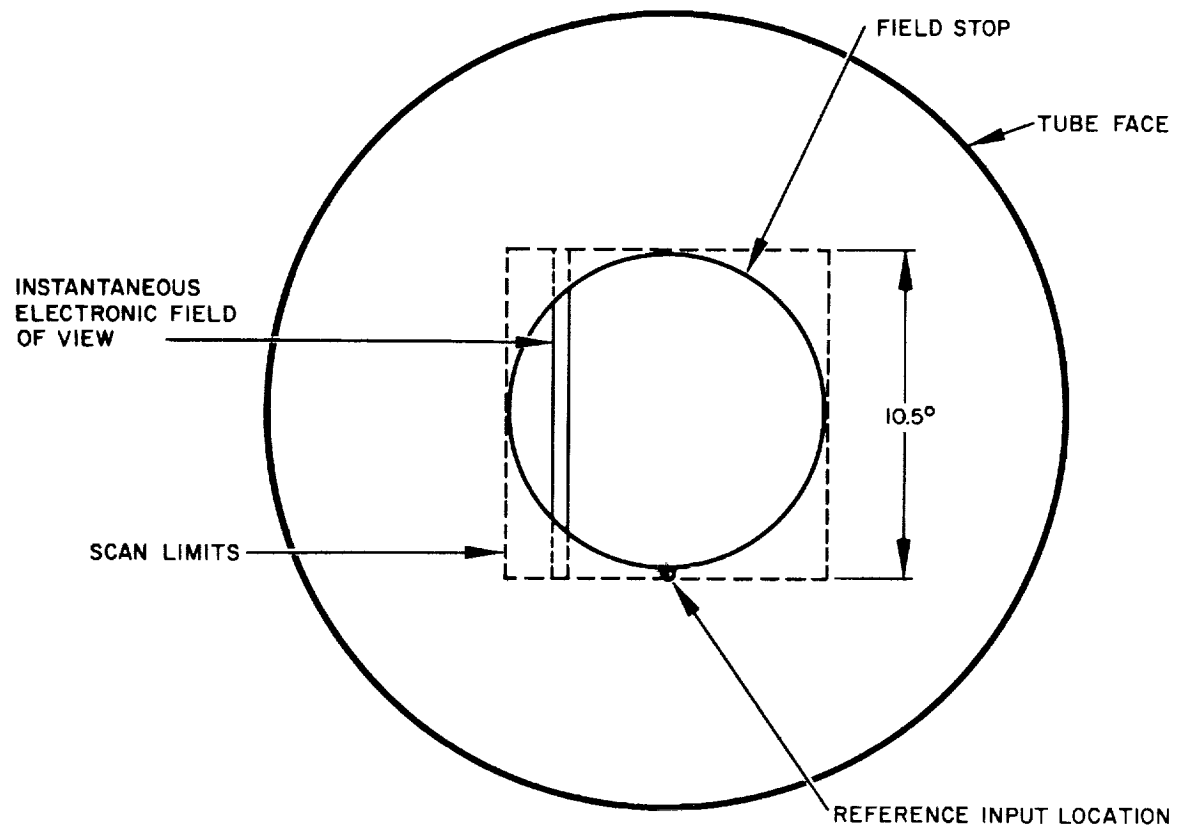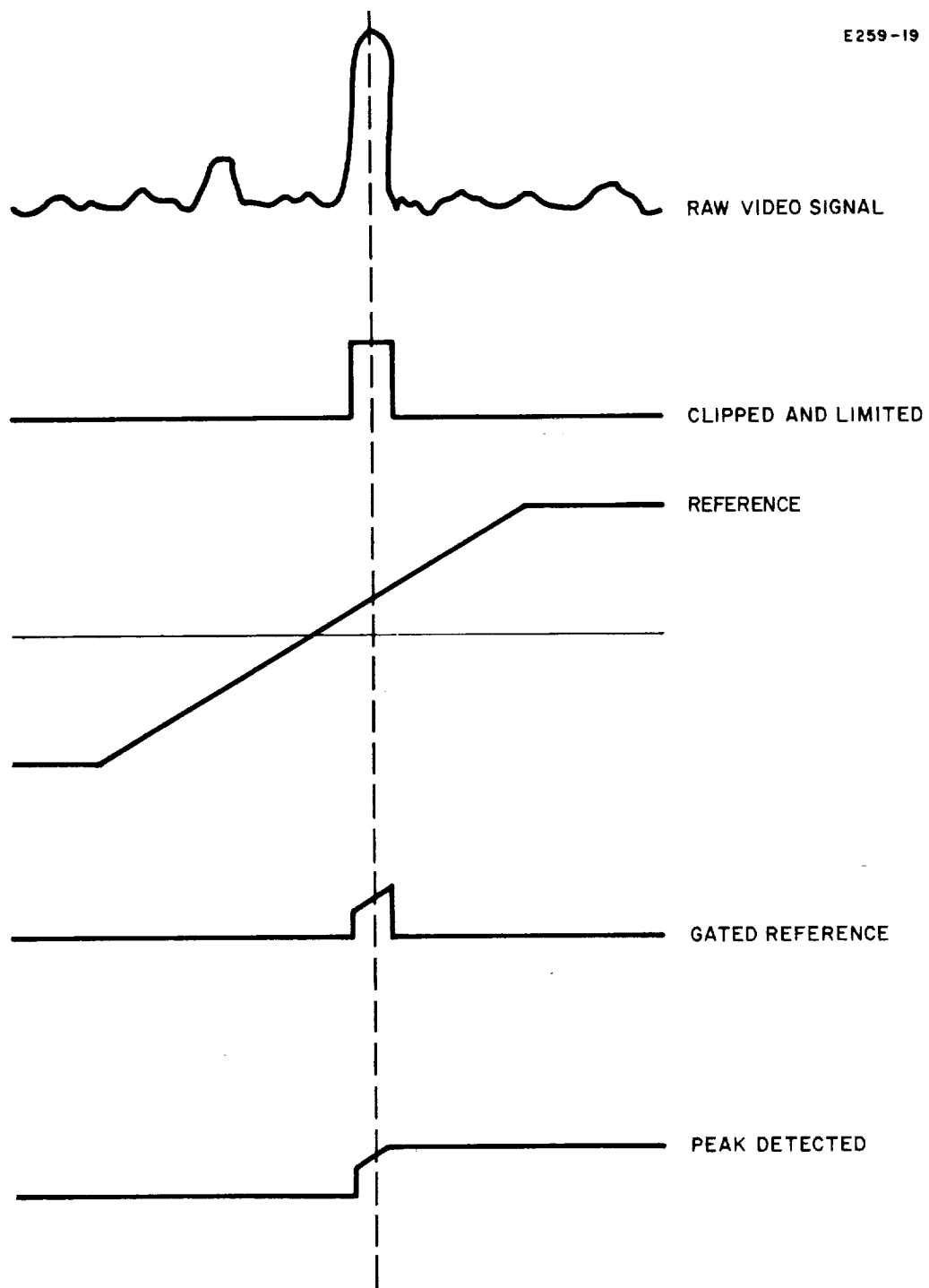ry provides a volume reduction in the image dissector tube and eliminates a voltage divider network and 14 dynode connections at the tube; however, the net result does not appear to favor use of the channel multiplier tube.

The signal processing electronics of the Bendix, ITT, and SBRC sensor designs employ some form of level detection to measure an "analog" of the time interval between start of a scan and detection of Polaris. This time interval may be represented by a pulse count, or a pulse width, or a pulse location with respect to a reference signal. The termination of the pulse count, pulse width, or pulse location is dependent on the pulse shape and stability and also the characteristics of the noise superimposed on the information pulse. Suitable designs have been proposed to compensate for these effects to provide for

44

the required attitude accuracy; however, questions of long term circuit stability still remain.

The Barnes-JPL sensor design, which originally employed a form of peak detection, was revised when poor electron image resolution at the aperture produced wide and poorly defined video pulses. Resolution of the CBS image dissector tube has been improved by redesigned wide angle electron optics since this design problem; however, no information has been obtained to indicate if the change alleviates the peak detection problem.

The Barnes-JPL sensor design appears to be less sensitive to video pulse shape since the error information is contained in the video pulse spacing and the effect of noise superimposed on the star pulse is reduced.

The Barnes-JPL signal processing, therefore, provides the preferable design coupled with the CBS or ITT image dissector tube, with the former tube perhaps being preferred because of previous development for equivalent sensors.

2.   Earth Sensor Systems

The candidate earth sensor designs to obtain attitude error information about the pitch and roll axis may be subdivided into mechanical scanning or modulating designs evaluated in Reference 1 and into a second group of sensors which employ no moving parts.

The former designs are typified by the Advanced Technology Laboratories' edge tracker sensor which utilizes oscillating optical elements to modulate the infrared energy received from the earth and focused on the detector. A thermistor bolometer detector is used. Modulation of the sensed radiation is required to enable discrimination of detector resistance change caused by radiation from resistance change caused by ambient temperature variation.

45

Although the ATL sensor design could be applied to the three-year synchronous orbit mission, the reliability of the position pivots through 2.8×10^{10} total cycles of operation is questionable.

Because of the nearly constant altitude of the synchronous orbit, the earth subtended angle is practically constant. The subtended angle varies approximately 7×10^{-4} degrees per nautical mile of orbital radius and the total variation of the orbital radius is determined by the 0.1 degree allowable station keeping error. The satellite longitudinal position error due to triaxiality of the earth will increase to 0.1 degree in 10 days. During this interval, the satellite velocity will change by 0.55 feet per second and the orbit radius change (ΔR) is given by

$$\Delta R \ = \ \frac{2}{w} \ \Delta v \approx 2.5 \qquad \text{(nautical miles)}$$

where

$\quad$ w $\quad$ = $\quad$ orbital angular rate (0.73×10^{-4} rad/sec)

$\quad$ Δv $\quad$ = $\quad$ orbital velocity change (0.55 feet/sec)

Therefore, the subtended angle of the earth is held constant to within 1.75×10^{-3} degrees by maintaining the required station keeping accuracy. This indicates that a detector array may be designed for a practically constant earth image size (as projected by an optical system) and that deviations of the image from the centered position will be equal to the pointing error of the sensor from the local vertical. Thus, with suitable detectors which will function without modulation of the received radiation, a mechanically passive sensor may be designed.

Discussion of Available Detectors

Radiation detectors are classified into image forming such as the photoemissive detector utilized in the image dissector tube and non-image forming detectors. In conventional photoemission, the escape energy to excite electrons from a solid into a vacuum is provided by incident radiation. This effect has been limited to

46

radiation in the low visible and ultraviolet wavelengths since the photon energy in the near and far infrared is insufficient to affect release of electrons. Field-induced photoemission employs an electric field to supply a part of the energy which an electron must have to escape from the solid and, therefore, opens up the possibility of relatively long wavelength infrared photoemission. Detectors of this type, which are now in an early state of development, could be employed in a sensor design similar to the Polaris star sensor.

Non-image forming detectors are subdivided into photo and thermal type detectors. The uncooled photo detector is useful to detect radiation up to approximately 3 microns wavelength. Supercooling of this detector extends the useful sensitivity range which could make them useful for far infrared detection. However, suitable long life cooling devices are not available at the present.

The thermal type detectors are classified as bolometers or thermocouples. In the bolometer type detector the thermally agitated molecules cause the resistivity of the detector to change in proportion to the incident radiation. In the thermocouple detector the thermally agitated molecules cause carriers to propogate generating a voltage proportional to the incident radiation.

Bolometers are operated with a bias voltage so that the change of resistance with radiation affects a change in the bias current flow which, in turn, provides a voltage signal. Bolometers are subject to Johnson, temperature and microphonic noise, which must be controlled in a sensor design. This type detector is subdivided into three groups including the semiconductor, superconductor, and metal bolometer. The thermistor bolometer, utilized for most space applications of infrared sensors to date, is a semiconductor device. This detector has a minimum detectable power level of 2×10^{-9} watts and has been developed to a high degree of ruggedness and reliability.

The thermistor bolometer is employed with a modulating device which chops the incident radiation to permit discrimination between the signal due to this radiation and the signal change caused by ambient temperature variation. Use of the detector in an unmodulated application has not been possible since the ability of a pair of bolometers (employed in a bridge circuit with one exposed and one shielded from the radiation) to track the temperature of a common heat sink has proven unsatisfactory. The two bolometers must track the heat sink temperature closer than the temperature change of the exposed element caused by the radiation, which is in the order of 10^{-4} $^{\circ}$C for earth sensors.

Superconductor bolometers require cooling to cryogenic temperatures for operation and are, therefore, not useful in long duration space applications.

The metal bolometer consists of a very thin, blackened metal strip, often platinum or nickel, which utilizes the temperature coefficient of resistance of metals in the range of 0.3 to 0.5 percent per $^{\circ}$C. Metal bolometer detector systems are able to detect bolometer element temperature changes in the range of 10^{-5} $^{\circ}$C. This is applicable for earth sensors, but fabrication tolerances present a difficult problem.

The thermocouple detector consists of a pair of similar bimetallic junctions; one being called the active junction and the other called the compensating junction. The active junction is exposed to the incident radiation while the compensating junction is shielded from radiation. Both junctions are mounted to a common heat sink, so that the compensating junction provides a reference from which the change in temperature of the active junction due to radiation may be determined.

To increase the signal or thermal voltage of the thermocouple, a group of junction pairs may be connected in series with all the active junctions exposed to the radiation. This combination

of thermocouples is called a thermopile. Original thermocouple detectors have been very fragile and used mainly in laboratories; however, recent emphasis on earth sensor instruments has resulted in design improvements so that this detector is useful for space application.

The thermocouple detector is compensated for ambient temperature variation by the compensating junction. The total signal is caused by the temperature difference between the two junctions, (i.e., by the temperature increase of the active junction caused by incident radiation). Thus, the detectors may be utilized without modulation of the radiation. The thermocouple has the disadvantage of having a sensitivity of approximately 0.25 times that of the thermistor bolometer.

The following sections describe earth sensor designs proposed by two companies qualified in the earth sensor development field. Several other sensors proposed for the synchronous orbit attitude sensor were similar to the mechanical scanning types described in Reference 1 and are not described here because of questionable capability of operating continuously for three years.

Barnes Engineering Co. Earth Sensor Design

The earth sensor design proposed by Barnes Engineering Co. (Reference 9) utilizes a thermopile detector and reflective optics which takes full advantage of the constant orbital radius to present a constant size image to the detector array.

Principle of Operation

The infrared image of the earth is reflected by a concave mirror to the detector. The detector consists of 120 active and 120 inactive thermocouple junctions. The active junctions are arranged in four groups of 30 each in a circular pattern. This circle coincides with the edge of the earth's image when the

satellite is at the synchronous orbit radius and the pitch and roll attitude errors are zero, or in other words, the design null position (see Figure 18). Error signals are generated when the earth's image is displaced from this null position, with the displacement resolved into pitch and roll attitude errors.

Optical and Detector Arrangement

The optical system consists of a 4" diameter f/1.5 uncoated lithium fluoride concave mirror. The mirror material averages 70 percent reflectivity in the 15 to 35 micron region. This operating wavelength range is selected to maximize radiation intensity available to the detector while minimizing the variation of this radiation caused by the earth characteristics previously discussed.

The only image defect which the mirror will have will be spherical aberration. This will provide a blurred image of the earth which is intended to aid in compensating for spatial radiation distribution anomalies as well as the earth's flatness at the poles. The concave mirror looks directly at the earth and reflects its image on the detector without the use of any other optics.

The detector consists of four groups of 30 active thermo-couple junctions which are positioned as shown in Figure 18. The active junctions are physically arranged and electrically connected to provide a signal proportional to the angular offset of the earth's image. The A and B surfaces of the thermocouple pair shown in Figure 19 form the active junctions. The output voltages of the detectors are plotted for earth movement from left to right. A signal similar to the total signal shown will be produced by the diametrically opposite detector pair.

The active junctions are coated black with the exception of the outboard detector at each end of a quadrant. These half-blackened junctions will provide a very small error signal for acquisition use when the center of the earth is within 16° of the

50

PITCH

EARTH IMAGE

ROLL

ROLL

40°

PITCH

40 ELEMENT THERMOPILE
DETECTOR ARRAY (4 SETS)
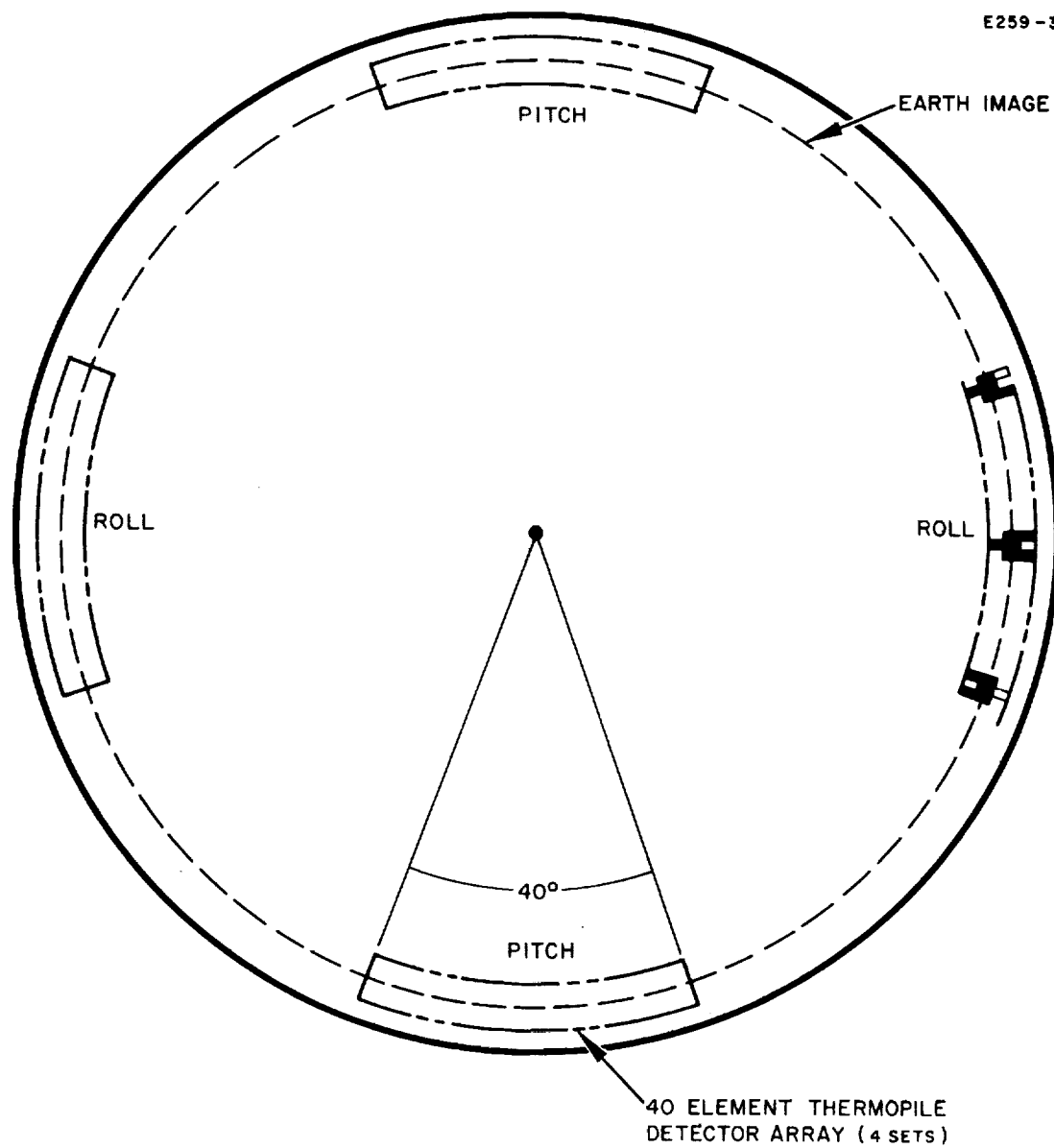
Fig. 18.   Image plane of the thermopile horizon sensor.

DETECTOR NO. 2 HALF BLACKENED

A

B

A

V_O

A

B

A

DETECTOR NO. I BLACKENED

V_O

NO. I
0

NO. 2

ACQUISITION
OFFSET

V_{p-p}

HOT EARTH LEFT, COLD SKY RIGHT

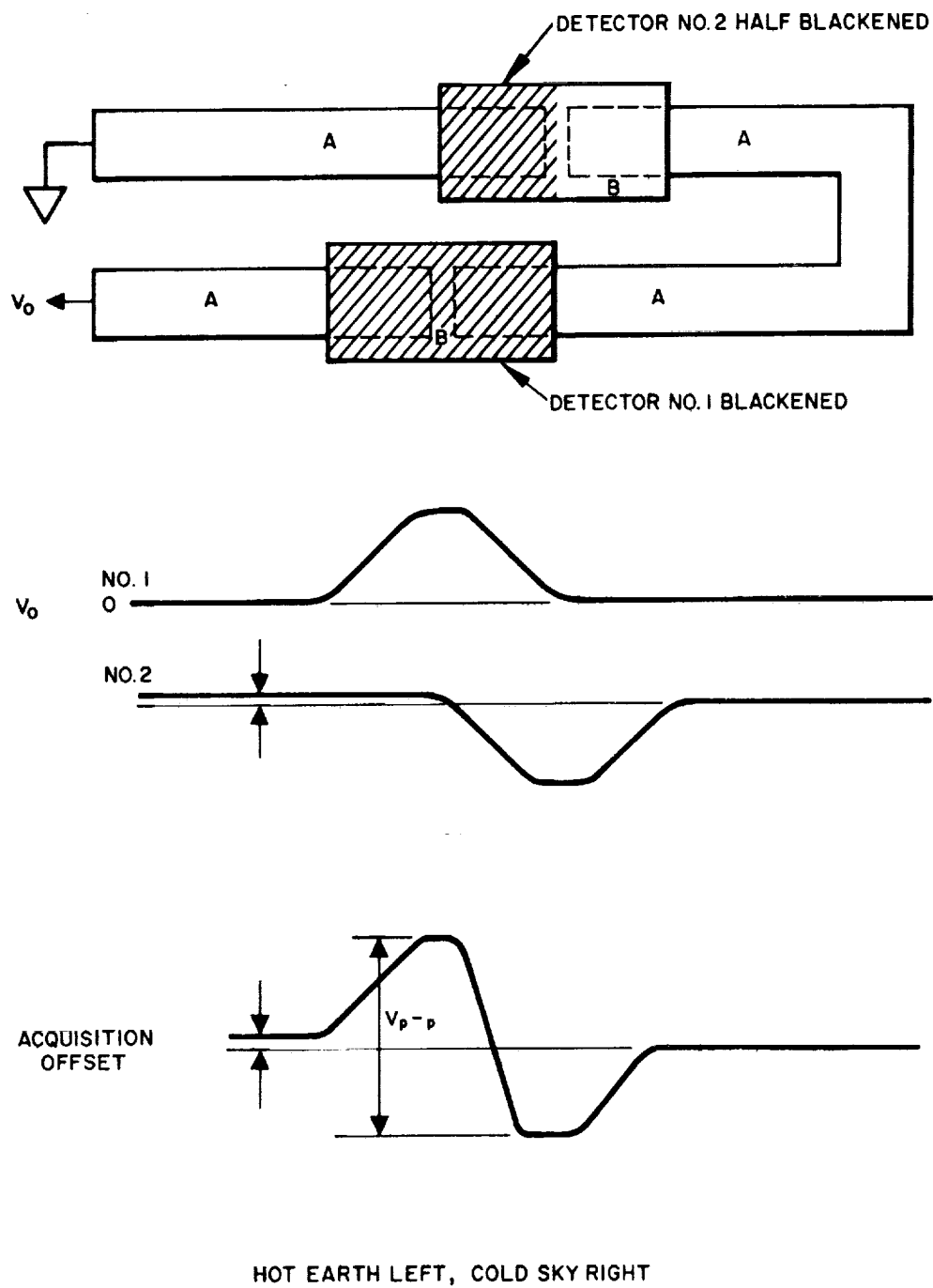Fig. 19. Simplified thermocouple output signal characteristics.

52

sensor axis. The general configuration of the sensor is illustrated in Figure 20.

Signal Processing

A functional block diagram of the sensor is presented in Figure 21. The output of the thermopile will go to a stable d.c. amplifier which has ultra low noise transistor preamplifiers and a photomodulator circuit employing neon lamps in conjunction with cadium selenide photoswitches. The lamps are used in a relaxation oscillator circuit to chop the d.c. signal from the preamplifiers. The actuating lamps also trigger the demodulating photoswitches assuring synchronism. This circuit has been successfully tested throughout the expected ambient temperature variations with an indicated stability of 0.1 microvolt. The total power consumption of the sensor is less than one-half watt.

The basic design of this earth sensor is relatively simple since mechanical modulation techniques and the resultant signal processing circuit complexity are eliminated. Manufacturing the detectors and the optics will require tight tolerances to assure sensor accuracy.

The sensor reliability will be determined by the MTBF of the thermopile and the solid state circuitry both of which are capable of attaining the required long duration of operation. Use of the thermocouple detector results in a lower sensitivity of the design; however, the large objective diameter, wide spectral bandwidth, and multiple element thermopile provide a satisfactory solution to this problem.

Kearfott Earth Sensor Design

The earth sensor proposed by Kearfott (Reference 10) utilizes refractive optics with a large objective lens to focus the constant size earth image directly on a metal bolometer.

Fig. 20. Thermopile earth sensor configuration.
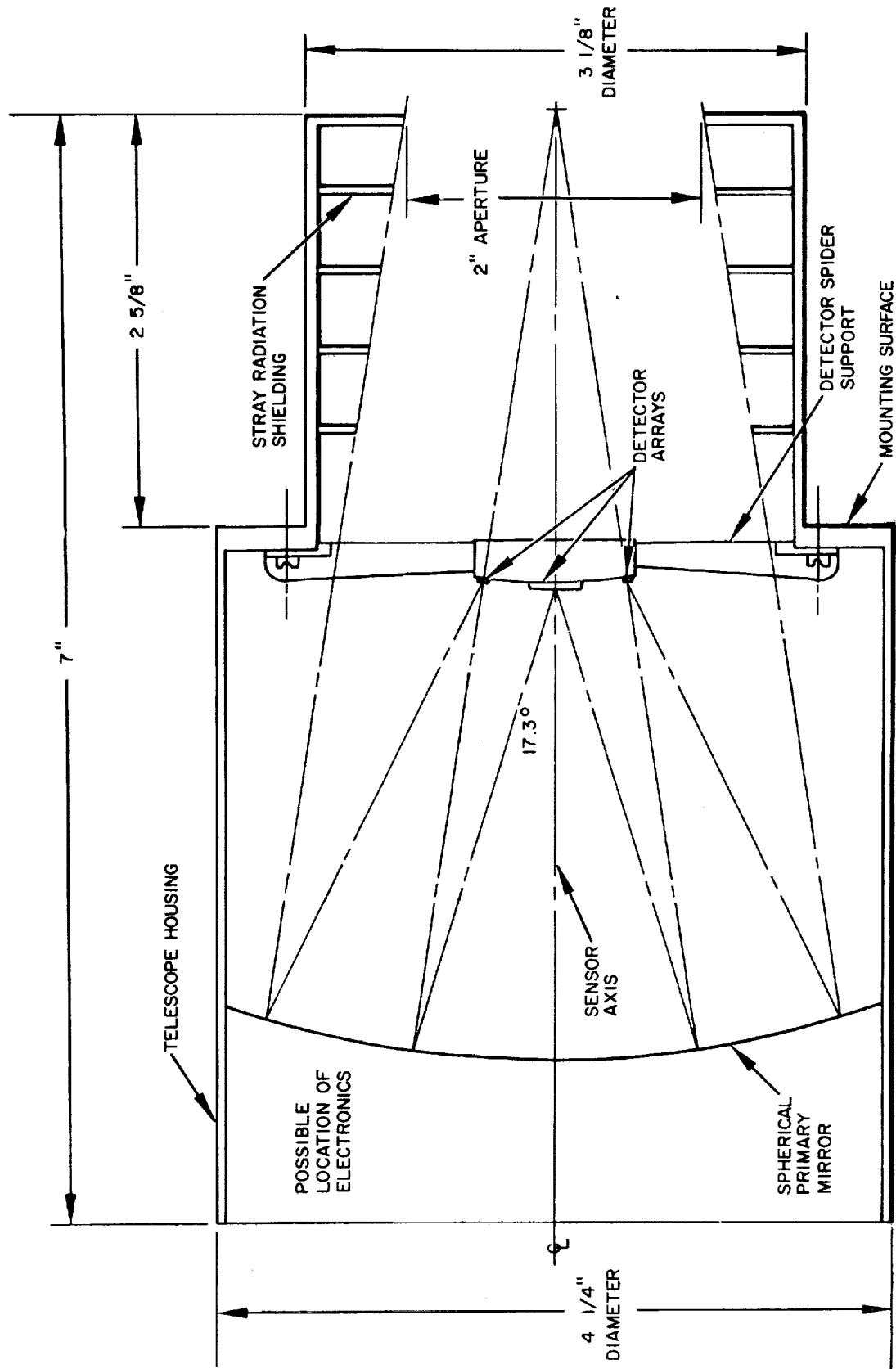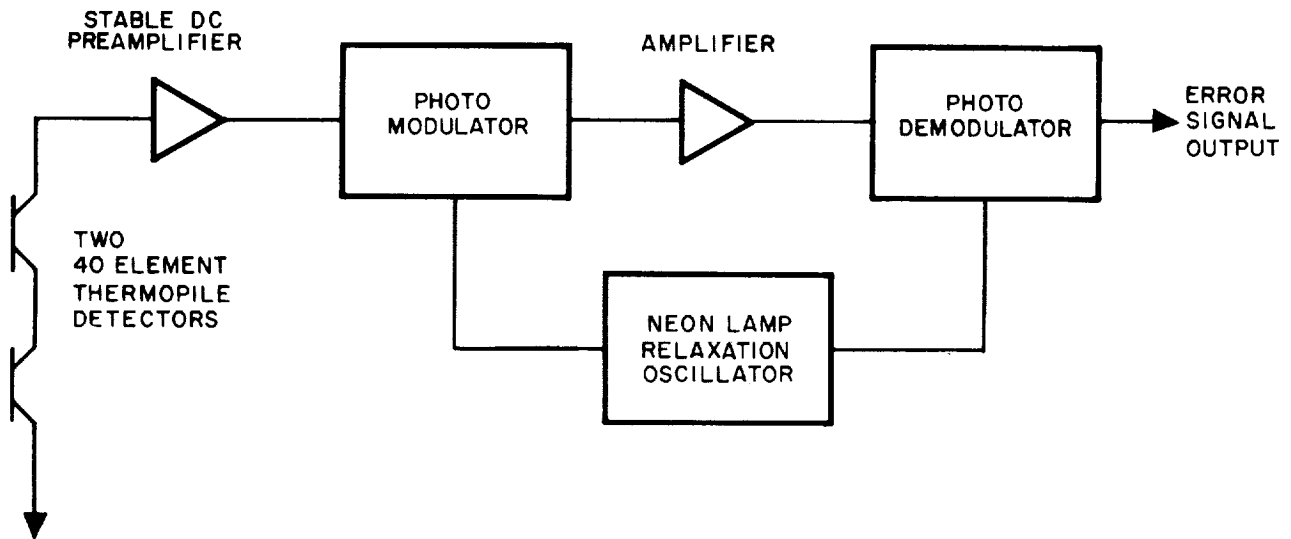
54

STABLE DC
PREAMPLIFIER

AMPLIFIER

PHOTO
MODULATOR

PHOTO
DEMODULATOR

ERROR
SIGNAL
OUTPUT

TWO
40 ELEMENT
THERMOPILE
DETECTORS

NEON LAMP
RELAXATION
OSCILLATOR

Fig. 21. Thermopile earth sensor functional block diagram.

Principle of Operation

Infrared radiated energy from the earth is received by the lens of the horizon sensor and focused directly on the detector. The detector has 16 electrical connections as shown in Figure 22. Four terminals identified 1, 2, 3, and 4 on one side are supplied with a.c. voltages of equal magnitude, but each with 90° phase displacement. The electrical grounds for these four terminals are identified 1^1, 2^1, 3^1, and 4^1. The eight connections, with their four power sources, supply the energy for one of the two attitude error channels while a similar configuration is used for the second channel. The four supply voltages for one axis of control, their grounds and their detector paths form an a.c. bridge. When the resistive paths through the detector are all equal (caused by 100 percent of the detector area being covered with infrared radiation, or a centered circle of infrared radiation), the voltages which are 180° out of phase with each other alternately supply and accept the voltages present. This condition balances the a.c. bridge and no current flows in the load resistor; therefore, zero error signal is produced. When the earth's image is projected on the bolometer and the image circle is not centered, unequal resistive paths are set up in the bolometer and currents flow through the ground paths creating voltages across the load resistor. By comparing the phases of the signal voltages with the phases of the supply voltages, a signal is obtained which is proportional to the physical displacement of the circular radiation pattern from the center of the bolometer.

Optical and Detector Arrangement

The optics consist of a germanium lens which focuses the infrared image of the earth on a metal bolometer as shown in Figure 23. The lens is designed to project the earth's image onto the bolometer slightly out of focus to integrate the effects of the earth's out-of-round and surface anomalies. The metal used for
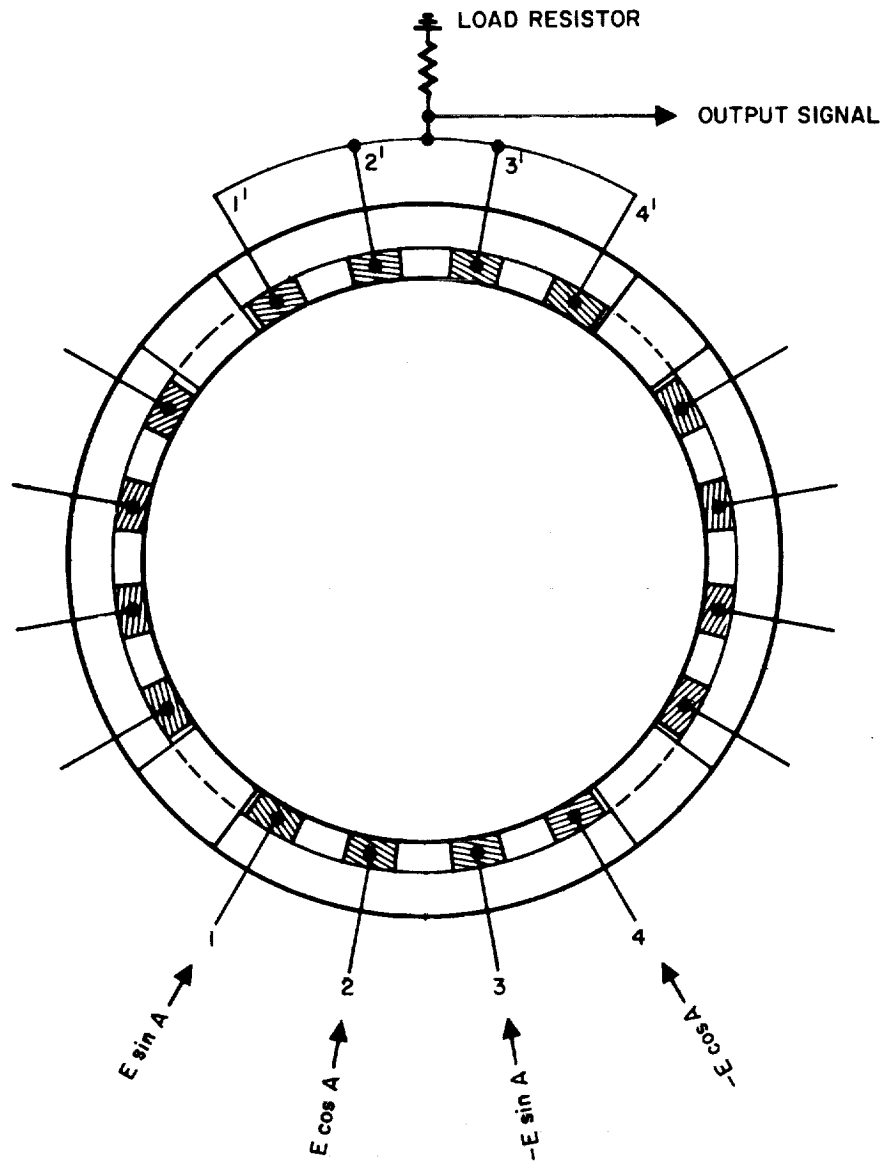
56

Fig. 22. Metal bolometer detector.

PLATINUM BOLOMETER

ELECTRONICS

ELECTRONICS AND
SENSOR BASE
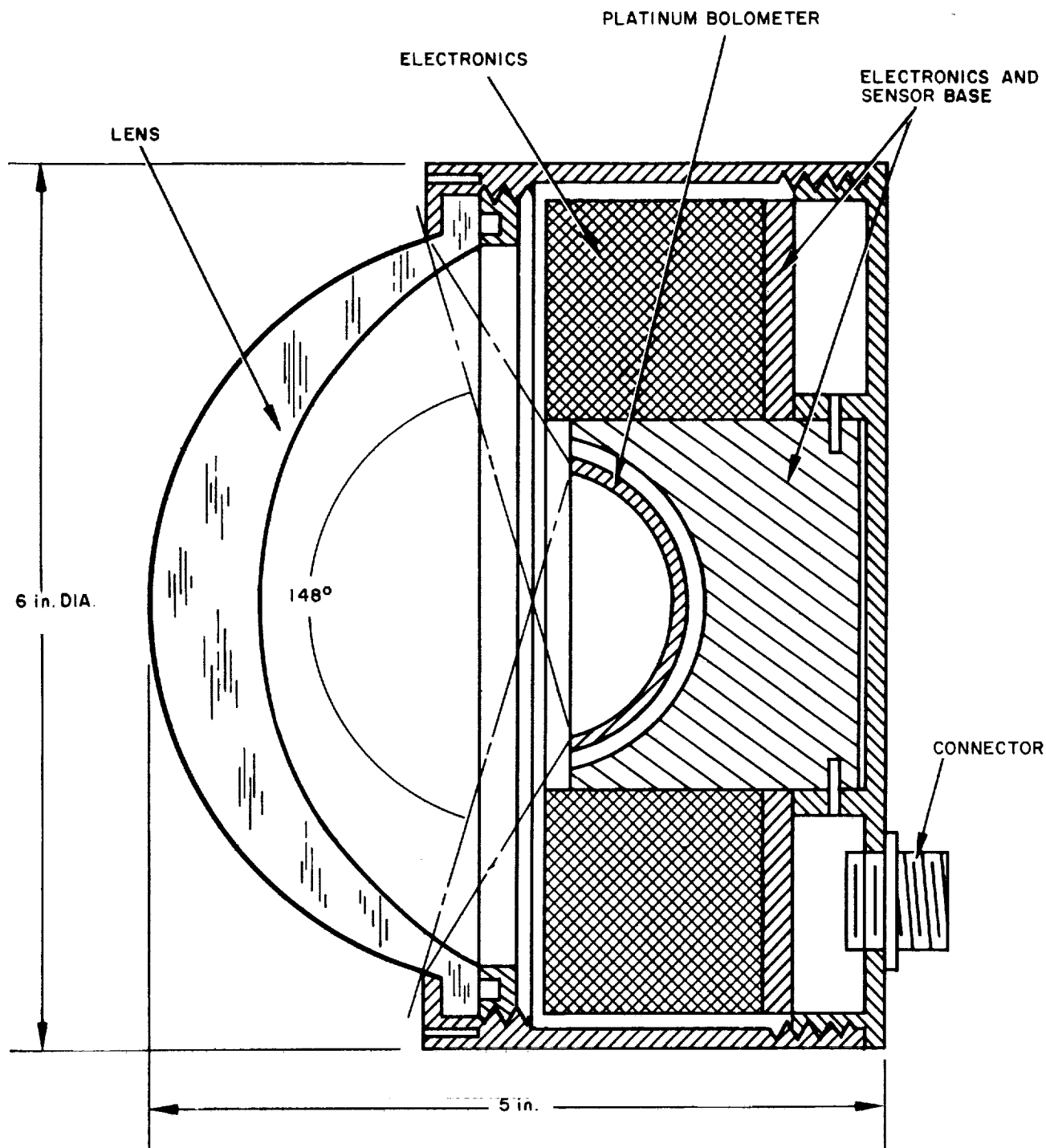
LENS

6 in. DIA.

148°

CONNECTOR

5 in.

Fig. 23. Metal bolometer earth sensor configuration.

the bolometer is platinum which is applied by an evaporative process with a "gold black" coating to increase infrared absorption of the bolometer. The platinum is one-half micron thick and is held to a very close tolerance to maintain a constant resistivity. The bolometer, which has an aplanatic hemispherical shape, is mounted at the focal point of the lens as shown in Figure 23.

Signal Processing Description

Figure 24 depicts the functional block diagram for the sensor. The voltage generator produces the four equal voltages with 90° phase displacements which are used for the two channels of detection. The voltage generator also supplies signals to the phase references for comparison in the phase detector with the amplified outputs from the summing load resistors. The phase detectors convert the phase relationship into low level analog signals which are amplified to provide the output attitude error signals.

The main advantage of this sensor design is the absence of moving parts which should provide a long life.

A disadvantage associated with this unit is the manufacturing tolerances associated with the platinum bolometer. Ambient temperature changes could be another problem area because metal bolometers are very sensitive to temperature changes. The sensor is designed to detect infrared radiation in the 8 to 15 micron wave length region which includes the most variable intensity spectral region (8 to 12 microns). This could result in large error signals caused by variations in the spatial distribution of radiation.

Comparison of Candidate Earth Sensors

A summary of the proposed sensor design characteristics are presented in Table III. The close proximity of the active and reference thermocouple junctions in the Barnes sensor decreases the design problems associated with maintaining the detector

VOLTAGE GENERATOR

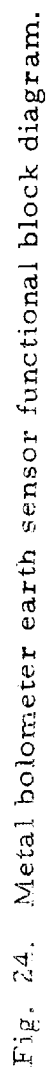PHASE REFERENCE

PHASE DETECTOR

ROLL ATTITUDE ERROR

PHASE DETECTOR

PITCH ATTITUDE ERROR

0° PHASE

90°

180°

270°

PRE-AMP

PRE-AMP

LOAD RESISTOR

LOAD RESISTOR

DETECTOR

OPTICS

Fig. 24. Metal bolometer earth sensor functional block diagram.

TABLE III

CANDIDATE EARTH SENSOR DESIGN CHARACTERISTICS

Characteristic	Barnes	Kearfott
1. Optical System		
Type	Reflective	Refractive
Aperture Diameter (in)	2.0	5.0
f/Number	1.5	0.6
Transmissivity	0.7	0.8
Total field of view (deg)	18	60
Spectral Bandpass (microns)	15 to 35	8 to 15
2. Detector Type	Thermopile	Metal Bolometer
3. Physical Package		
Outline Dimensions (in)	4.25 dia. x 8.0 Length	6.0 dia. x5.0 length
Total weight (pounds)	2.25	3.9
Power consumption (watts)	0.5	5.0

elements at the same ambient temperature to prevent erroneous detector signals. The same condition does not exist for the metal bolometer detector; therefore, thermal design will be more critical. The weight and power requirements of the Barnes sensor design provide an advantage over the Kearfott sensor. The relative added complexity of the Kearfott signal processing system will make achievement of high reliability more difficult.

D. Recommendation for Sensor Subsystem

The preceeding discussion has shown that the sensor subsystem requirements of the ion engine control system for a synchronous orbit satellite may be satisfied by available star and earth sensor designs. The evaluated sensors are all mechanically passive devices so that long term operational reliability is determined by the capability of the manufacturer to develop detectors and solid state circuitry with sufficient mean time between failure; problems which are amenable to solution by established procedures.

In the case of the Polaris star sensor, the most appropriate design selection appears to be an adaptation of the Barnes-JPL Canopus Sensor. This design has completed a development cycle in the Mariner C spacecraft program which has resulted in several improvements in the CBS image dissector tube design and the sensor signal processing circuitry. The modifications required of this sensor would involve changing the total field of view (i.e., changes in optics and sweep circuitry) and changing the video threshold detection circuitry to function with Polaris effective radiant intensity level.

To cancel the $\pm$ 0.8 degree daily yaw oscillation caused by the declination of Polaris, a bias voltage generator will be required which is synchronized to the orbital period. This generator would produce a voltage, which when added to the yaw error signal produced by the Polaris sensor would cancel the periodic angular deviation of

the line of sight to Polaris from the normal to the orbital plane.
The voltage function (V) generated would be

$$V = V_o \sin \left(\frac{2\pi t}{\tau} \right)$$ \hfill (volts)

where

V_o = max bias voltage (0.8 degree x 2 volt/degree = 1.6 volt)

τ = sidereal orbital period (sec)

t = orbital time (sec)

One possible mechanization of this device consists of a master oscillator, a binary counting train, a digital to analog converter, and a narrow fan-beam shaped sun sensor. The master oscillator would supply pulses to the counter and, therefore, the stored count would be proportional to the elapsed time. The converter would produce the analog bias voltage proportional to the stored count to be summed with the sensor attitude error signal. The sun sensor "zeros" the counter at the completion of each solar day. The actual "zero" count is the stored count that gives a zero output analog voltage. The "zero" count would be advanced approximately 1/365 of the total counter storage capability each time the counter is reset to account for the average variation of the mean solar day and the sidereal day.

The added complexity of this function generator may be eliminated if the allowable yaw attitude error is increased to $\pm$ 1.3 degrees, which may be suitable for certain missions of the satellite.

The proposed Barnes earth sensor design appears to be the best selection to obtain pitch and roll attitude error signals; basically because a higher confidence level is placed on the thermopile detector when compared to the metal bolometer. This detector has been subjected to extensive development for space applications with emphasis being placed on increasing the ruggedness of the

63

unit and improving thermocouple fabrication techniques. Preliminary design and breadboard testing of the signal processing circuitry has also been performed to ascertain that the required stability could be achieved.

The sun and moon interference with the earth sensor operation must be compensated for by circuitry that will reject detector error signals above a certain level. Thus, when the interfering radiation falls on a thermopile sector, the resultant large detector signals will be prevented from entering the signal processing circuits. The sensor error signal of the affected channel will indicate zero attitude error during this blanking period and the satellite attitude will drift. If the effective angle subtended by the sun or moon in the spectral wavelength of the sensor is considered to be 1 degree, then the total blanking period will not exceed approximately 4 minutes and the attitude error of the affected axis will change by approximately 0.72 degree.

The attitude drift during interference of an earth sensor channel by the sun will cause the attitude excursion to exceed the required deadband. Standby integrating rate gyros will be required unless relaxation of the permissible attitude error is obtained. Gyros of the type discussed in a previous section will be capable of supplying the attitude error signal during the period of earth sensor blinding.

III.   SYSTEM SIMULATION STUDY

A.   Low Altitude Mission Analog Simulation

A preliminary report on the low altitude mission simulation results is presented in References 1 and 11. The purpose of this preliminary analog investigation was to aid in the selection of candidate attitude sensors for the mission and to determine the degradations of system performance due to the filtration necessary to suppress expected sensor noise inputs. Ideal, linear sensor output signals containing discrete levels of white noise were assumed for the preliminary simulation. The results of this study assisted in the recommendation of a sensor subsystem. The details of the study results and recommendation are given in References 1 and 11.

The final analog study involved utilizing the noise and dynamic response characteristics of the recommended sensor and investigating the effects upon system performance due to sensor nonlinear characteristics. The characteristics simulated in addition to noise inputs were: 1) null shift (constant bias); 2) null drift (low frequency sinusoidal drift; 3) sensor dynamic response characteristics; and 4) sensor linearity (gain) variation.

(1)   Description of Simulated System

The attitude sensor characteristics are represented in the block diagram of Figure 25, which also indicates the single axis control system model utilized in this simulation.

The analog simulation diagrams for the system are given in Figures 26 and 27. Typical vehicle parameters which were utilized in the simulation are given in Table IV.

The values and ranges of values of the simulated sensor characteristics and required noise filtration are given in Table V. The thrust characteristics were assumed to be square wave for the convenience of simulation.
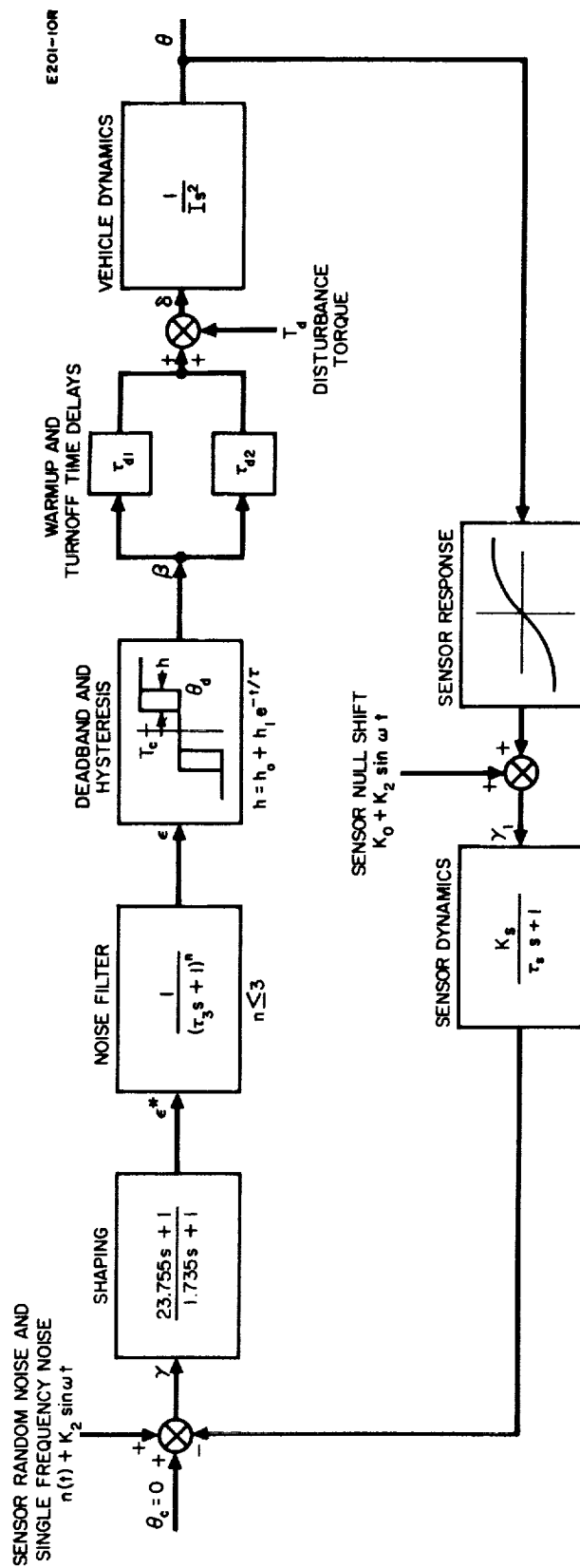
Fig. 25. Single axis control system model including sensor noise characteristics.
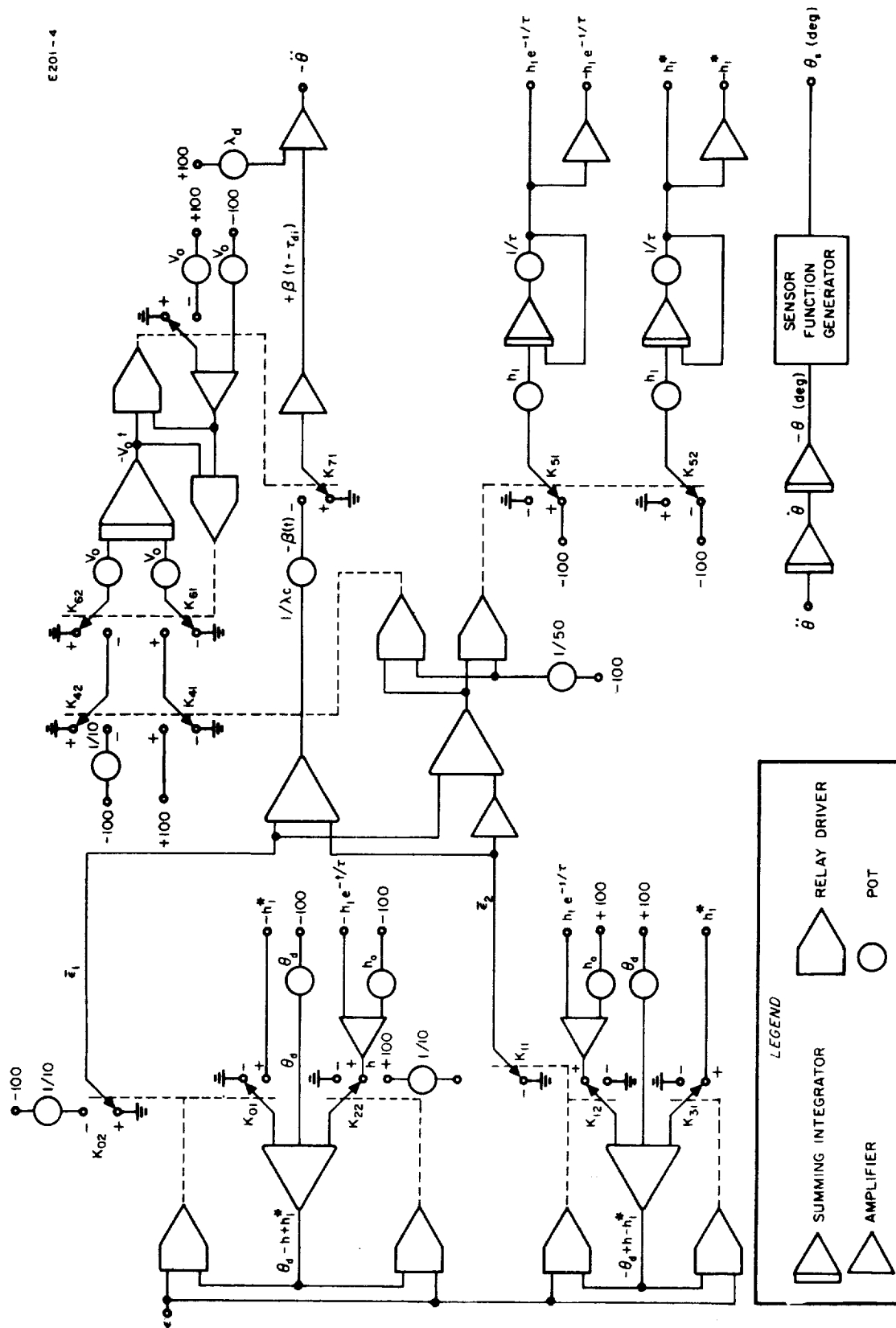
66

Fig. 26. Simulation diagram of deadband switch, hysteresis, switch kick, time delay, and vehicle dynamics.
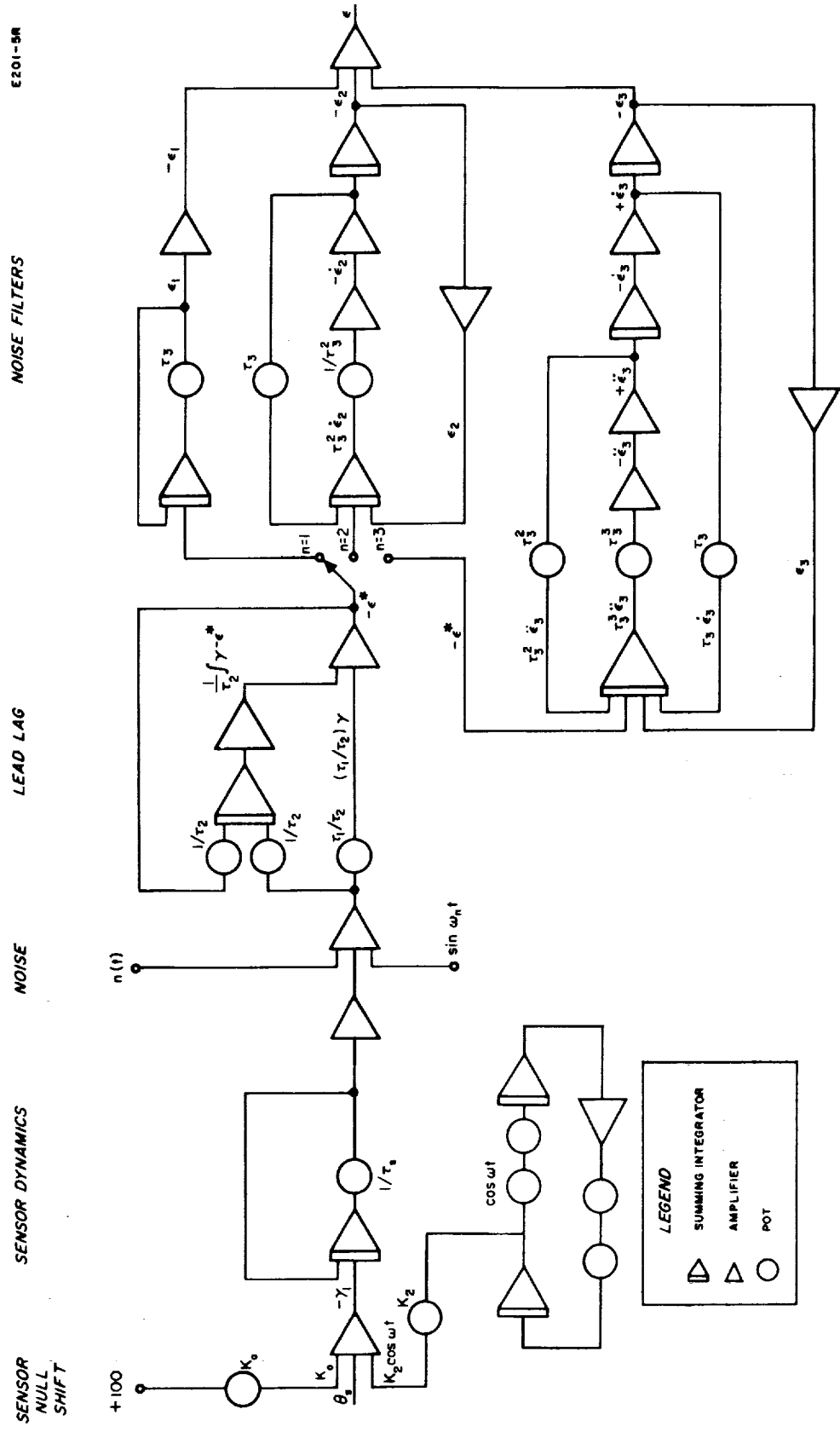
67

Fig. 27. Simulation-diagram of sensor null shift and drift, sensor dynamics, noise, lead-lag, and noise filters.

68

TABLE IV

SIMULATED VEHICLE PARAMETERS

θ_d	(attitude deadband)	± 2.0 degrees
λ	(control acceleration)	6.25×10^{-5} rad/sec^2
I	(moment of inertia)	12 slug-ft^2
T	(control torque)	$.75 \times 10^{-3}$ ft-lb
P_c	(continuous power required)	25 watts
P_T	(thrusting power)	160 watts
$d_s P_s$	(average station keeping power)	32 watts
$P_w T_w$	(warm-up energy)	.75 watt-hr
P_a	(nominal average power)	94 watts
τ_1	(lead time constant)	23.755 seconds
τ_2	(lag time constant)	1.735 seconds
h_o	(steady state hysteresis)	0.04 degree
h_1	(switch-kick amplitude)	1.0 degree
τ	(switch-kick time constant)	10.0 seconds

TABLE V
RANGES OF ASSOCIATED SENSOR PARAMETERS

Required noise filter	$1/(.11s + 1)^2$
Sensor Dynamic Response	$1/(.1s + 1)$
White noise rms output, n (t)	0.024 degree rms
Sensor bias, K_o	0 - 0.25 degree
Sensor sinusoidal drift amplitude, K_1	0 - 1.0 degree
Sensor sinusoidal drift frequency, ω	0 - 0.01 rad/sec
Sensor gain variation, K_s	1.7 - 0.5
Disturbance torque ratio, T_d/T_c	0 - 0.2

(2) Results of Low Altitude Simulation Study

A detailed discussion of the effects of noise, the required noise filtration, and the switch-kick mechanism are given in Reference 1. The noise filtration in conjunction with the switch-kick has been chosen to eliminate all noise pulses on the warm-up

command signal due to temperature shock considerations on the ionizer. The following sections will illustrate the effects of the various sensor characteristics and vehicle disturbance torques acting on the system which has been determined (Reference 1) will meet the noiseless ionizer warm-up requirement for a white noise (rms) equivalent input of 0.024 degree.

The various sensor characteristics were simulated separately in the system and also combined with a group of simultaneous effects. The noise inputs, noise filtration, and sensor dynamic response were not varied due to the preliminary nature of the computer study and the recommended sensor specifications. Information on characteristics other than noise and dynamic response were not available prior to actual laboratory and flight test of a sensor model; hence, typical ranges for variation of the parameters were chosen in order to determine the effects on system performance for the low altitude mission.

(3)   Effect of Sensor Noise Input to System

The system performance is most readily demonstrated by a phase plane portrait (θ vs $\dot\theta$) for the system recorded directly from the computer. The system operation with the addition of .024 degree rms white noise to the simulated system (sensor response and noise filtration included) is illustrated by the phase plane plot of Figure 28. The outer trajectory represents the nominal noiseless, disturbance-torque-free limit cycle, which has a limit cycle rate of .0155 deg/sec and an average power figure of merit of 103.0 watts.

The inner trajectories of Figure 28 represent the system performance with the addition of .024 degree rms white noise. The thrusting pulse is reduced somewhat due to the effect of the filtered noise reducing the effective hysteresis at thrust on and thrust off. (This effect is discussed in more detail in Reference 1.) The trajectory no longer is a singular distinct limit cycle, but is
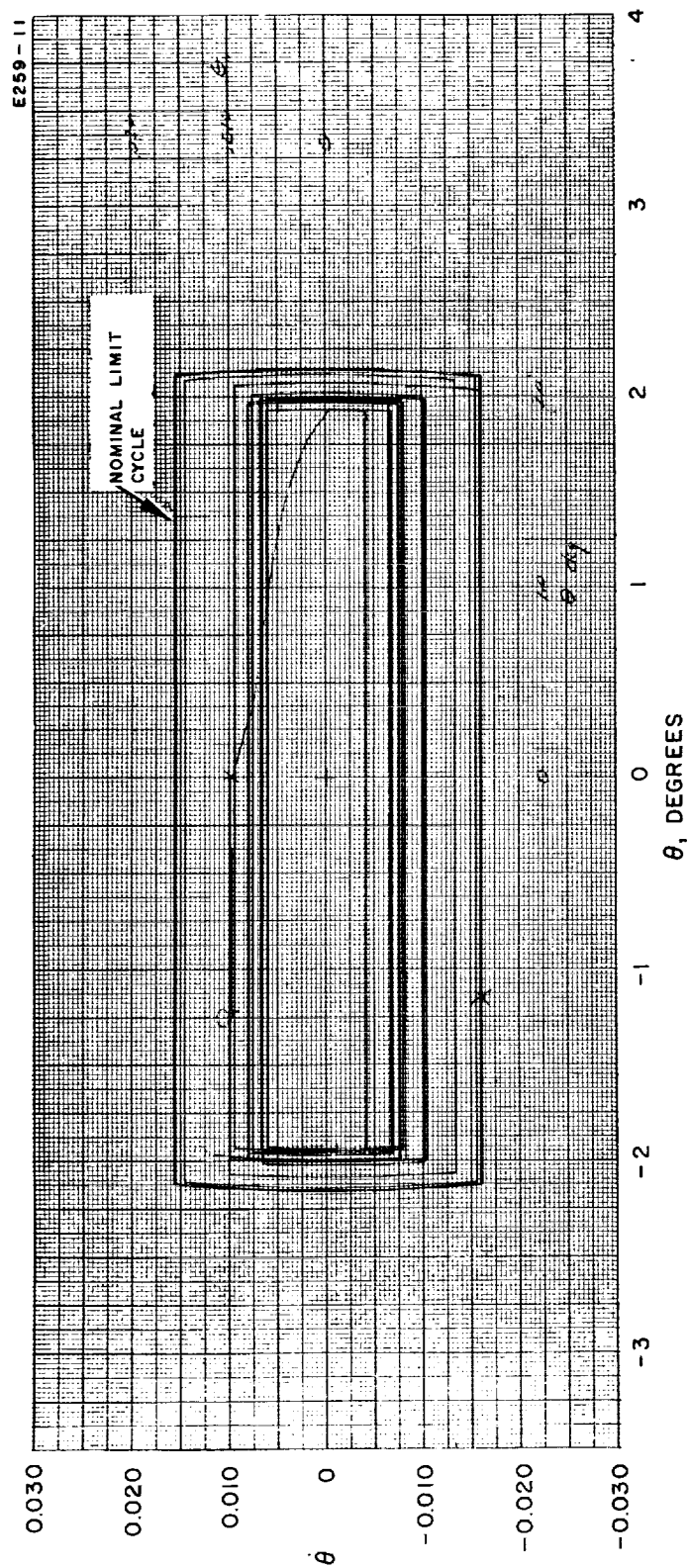
NOMINAL LIMIT
CYCLE

θ, DEGREES

$\dot{\theta}$

0.030

0.020

0.010

0

-0.010

-0.020

-0.030

Fig. 28. Phase plane plots showing the effect on system performance caused by 0.024° rms noise.

71

a range of trajectories which do not diverge or converge significantly. The vehicle rates ranged from .0060 deg/sec to .095 deg/sec in this mode. No single power figure of merit can be assigned for the system operation in the presence of noise, but for comparison purposes, a range may be assigned for a single operation half cycle. For this case, the figure of merit ranges from 71.5 watts to 82.3 watts, verifying the ability of the filtered noise to improve system performance in the disturbance torque-free case by effectively reducing hysteresis.

(4)   Effect of Sensor Null Shift

The addition of a constant sensor null shift did nothing more than shift both noise-free limit cycles and noise presence phase trajectories away from the desired null. Neither limit cycle rates nor the average power figures of merit were significantly different than those in the previous case. The phase plane trajectories for K_o = 0 degree, 0.1 degree, and 0.25 degree in the noise-free case are shown in Figure 29, and those for the noise present case are shown in Figure 30 for the same values of K_o.

Sinusoidal sensor null drift of the type that might be encountered, due either to electronic drifts or target (earth) variations with time, were inserted into the control loop with little degradation of system performance. In actuality, this effect is nothing more than the insertion of a low frequency, pure sinusoidal noise input. This low frequency "noise" caused a somewhat more pronounced variation in the rate amplitude of the phase trajectories as is illustrated by the phase plane portraits of Figure 31. The dashed line trajectories represent a system with no sensor null drift, while the the solid line trajectories represent the addition of a sinusoidal null drift of $K_1 \sin \omega t$, with K_1 = 0.1 degree and ω = .01 rad/sec. This particular choice represented a peak drift rate of .001 deg/sec, or approximately 10 percent of the ideal (no noise filter, ideal sensor response) limit cycle rate for the mission. The amplitude of the sinusoidal null drift
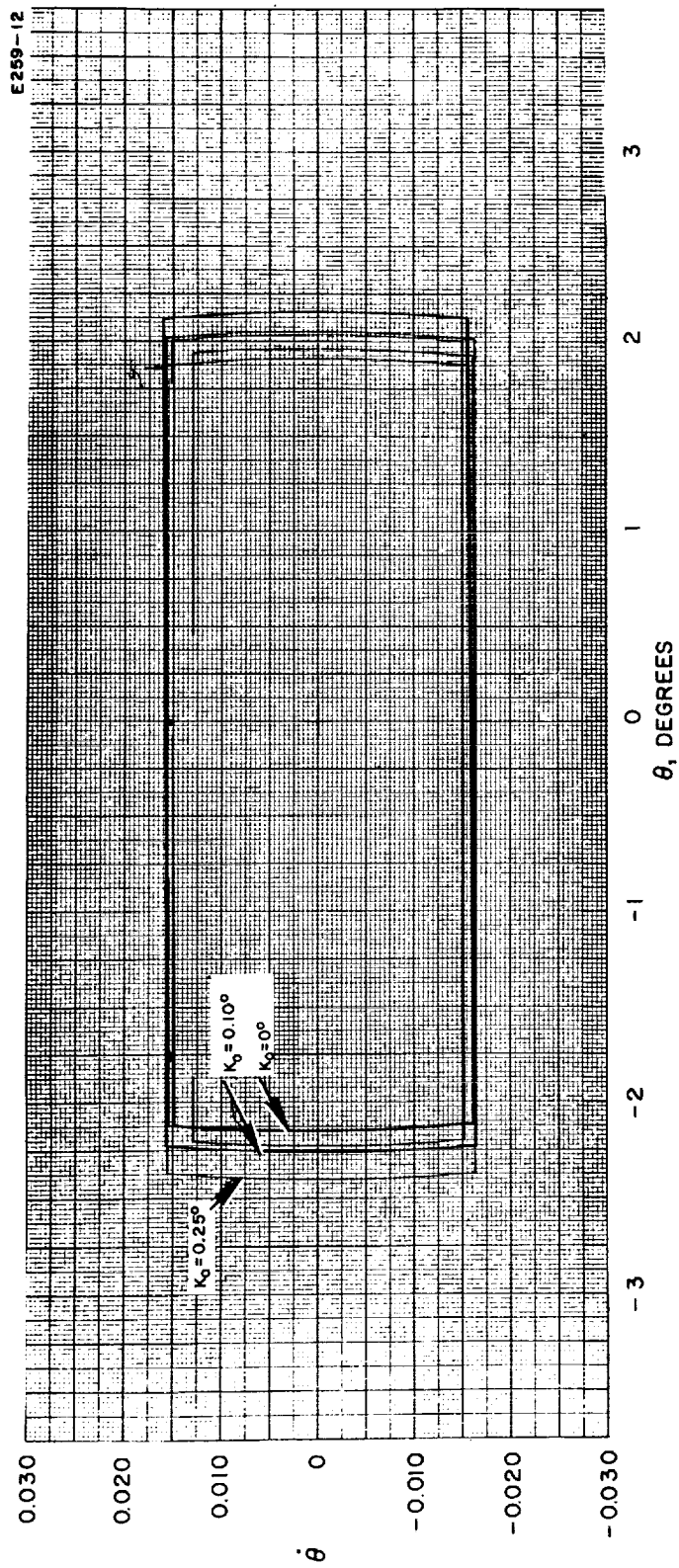
72

Fig. 29. Phase plane plots showing the effect on system performance caused by sensor null shifts of 0.1° and 0.25° (zero noise).
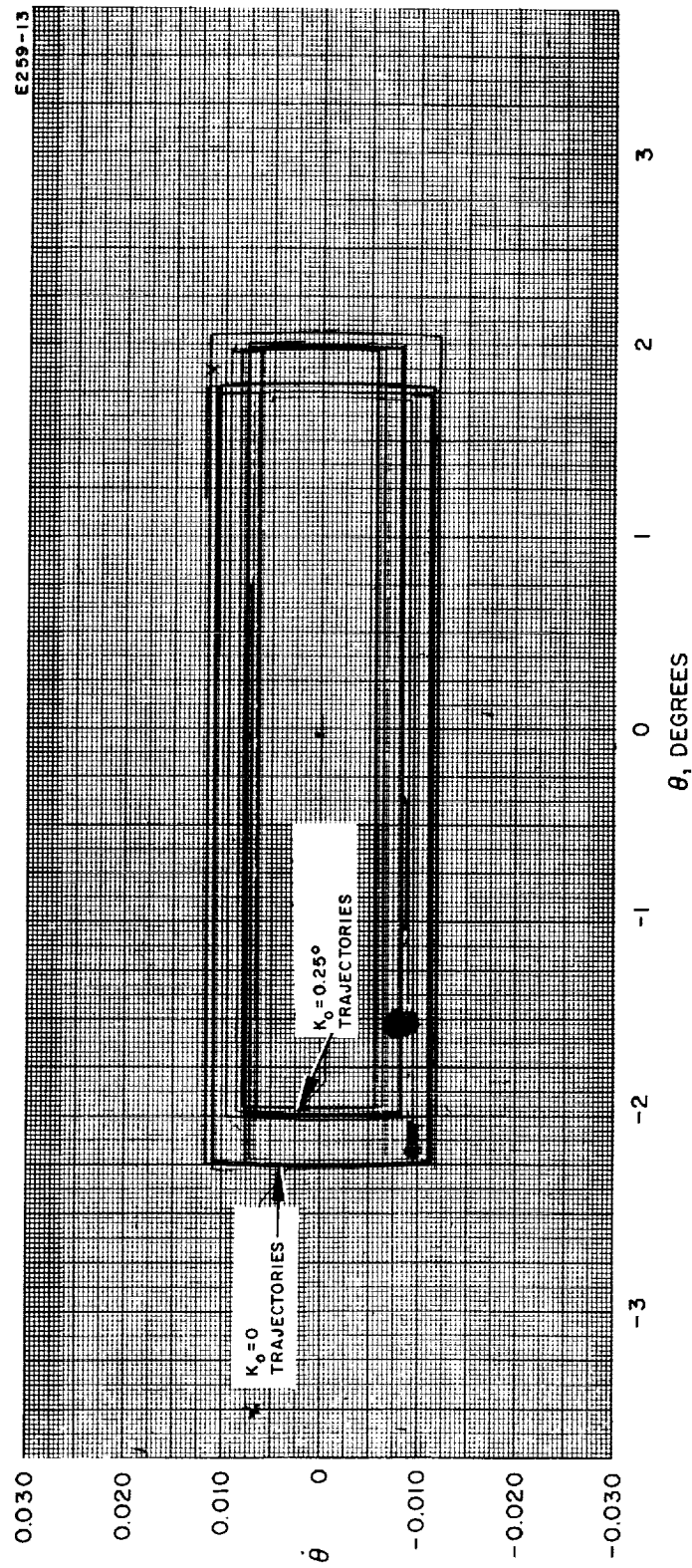
Fig. 30. Phase plane plots showing the effect on system performance caused by a sensor null shift of 0.25° and 0.024° rms noise.
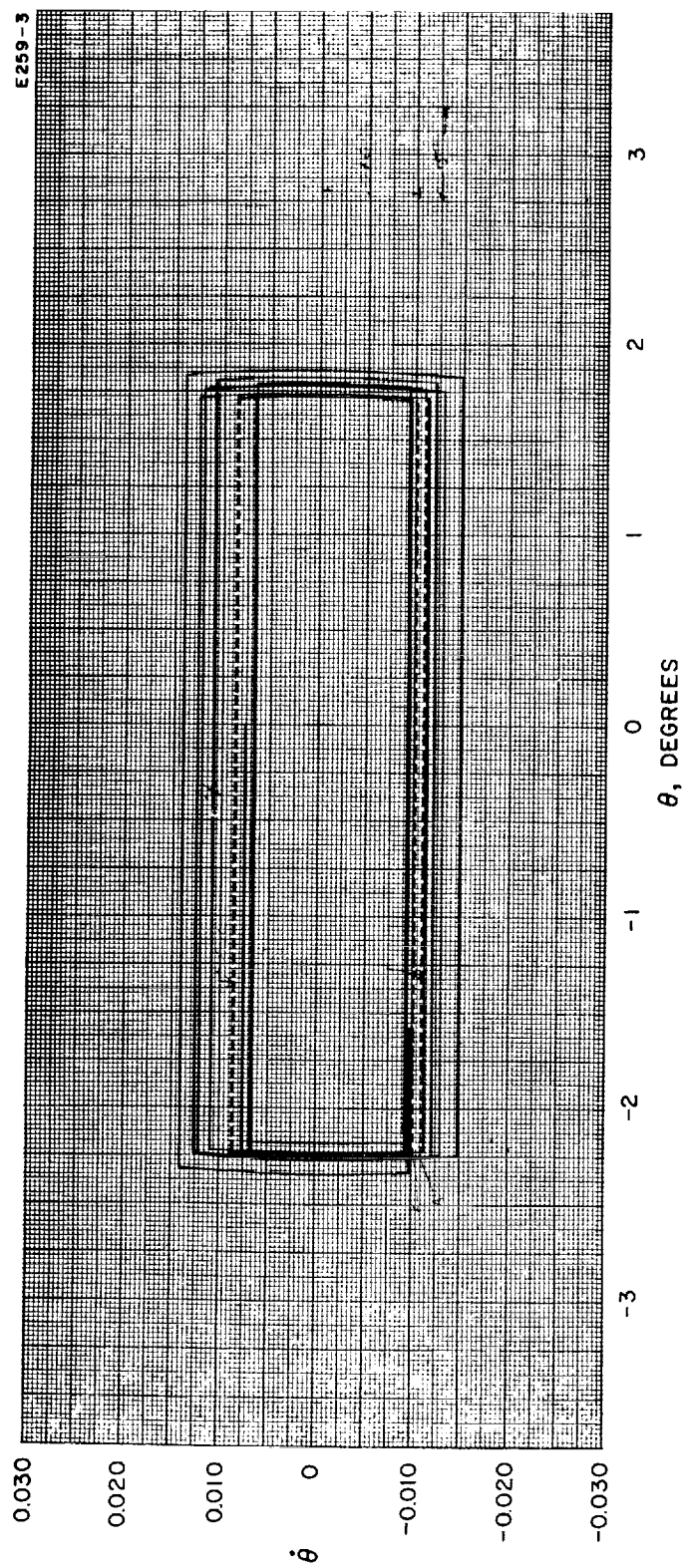
74

Fig. 31.   Phase plane plots showing the effect on system performance caused by a sinusoidal null drift of 0.1° sin (0.01 rad/sec) t.

75

input was then increased to 0.25 degree, again resulting in some-
what more variation both in the θ and $\dot{\theta}$ axes of the phase trajectories
than without the sinusoidal input; however, the long term stability
of system performance was again adequately demonstrated for this
mode.

The sinusoidal null drift was subsequently increased in
amplitude to K_1 = 1.0 degree, and decreased in frequency to
ω = .001 rad/sec (approximately the orbit rate). The resulting
phase plane is shown in Figure 32. The trajectory variation
between subsequent cycles is seen to be quite extreme; however,
again long term stability of system operation is demonstrated. Due
to the large (1.0 degree) amplitude, the vehicle sometimes exceeds
the ± 2.0 degree deadband while at other times operates well within
the deadband. The range of vehicle rates is seen to be from
.045 deg/sec to .0195 deg/sec for this phase trajectory.

(5)   Effect of Disturbance Torques

Constant disturbance torques were imposed upon the system;
the range of disturbance torque-to-control torque ratios being from
0 to 0.2 (a disturbance torque range of 0 to approximately 2000
dyne-cm). The noise-free limit cycles for K_o (null bias) = 0 and
0.25 degree and T_d/T_c = 0.04 (400 dyne-cm disturbance torque)
are illustrated by the phase trajectories on the right in Figure 33.
The limit cycle rate is 0.014 deg/sec in both cases and the power
figure of merit is 115.9 watts. The corresponding ideal limit
cycles for K_o = 0 and 0.25 degree and T_d/T_c = 0.20 (2000 dyne-cm
disturbance torque) are shown by the phase trajectories on the
left in Figure 33 (light line trajectories only). For this case, the
limit cycle rate is .027 deg/sec and the average power figure of
merit is 238.4 watts. (Preliminary studies have shown that the
maximum tolerable disturbance torque for the assumed vehicle
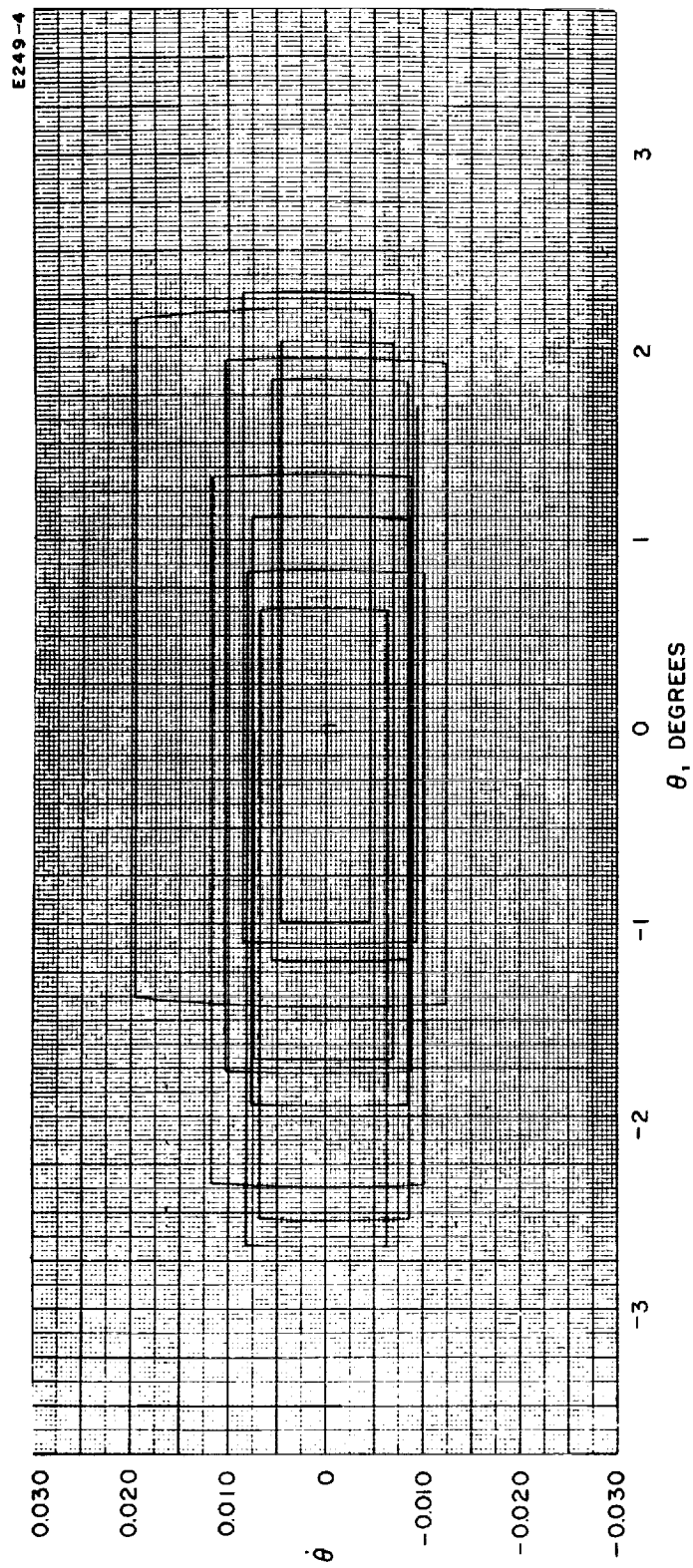is 525 dyne-cm in order that a 150 watt average power require-
ment is met.)

76

Fig. 32. Phase plane plot showing the effect on system performance caused by a sinusoidal null drift of 1.0° sin $(0.001$ rad/sec$)$ t.
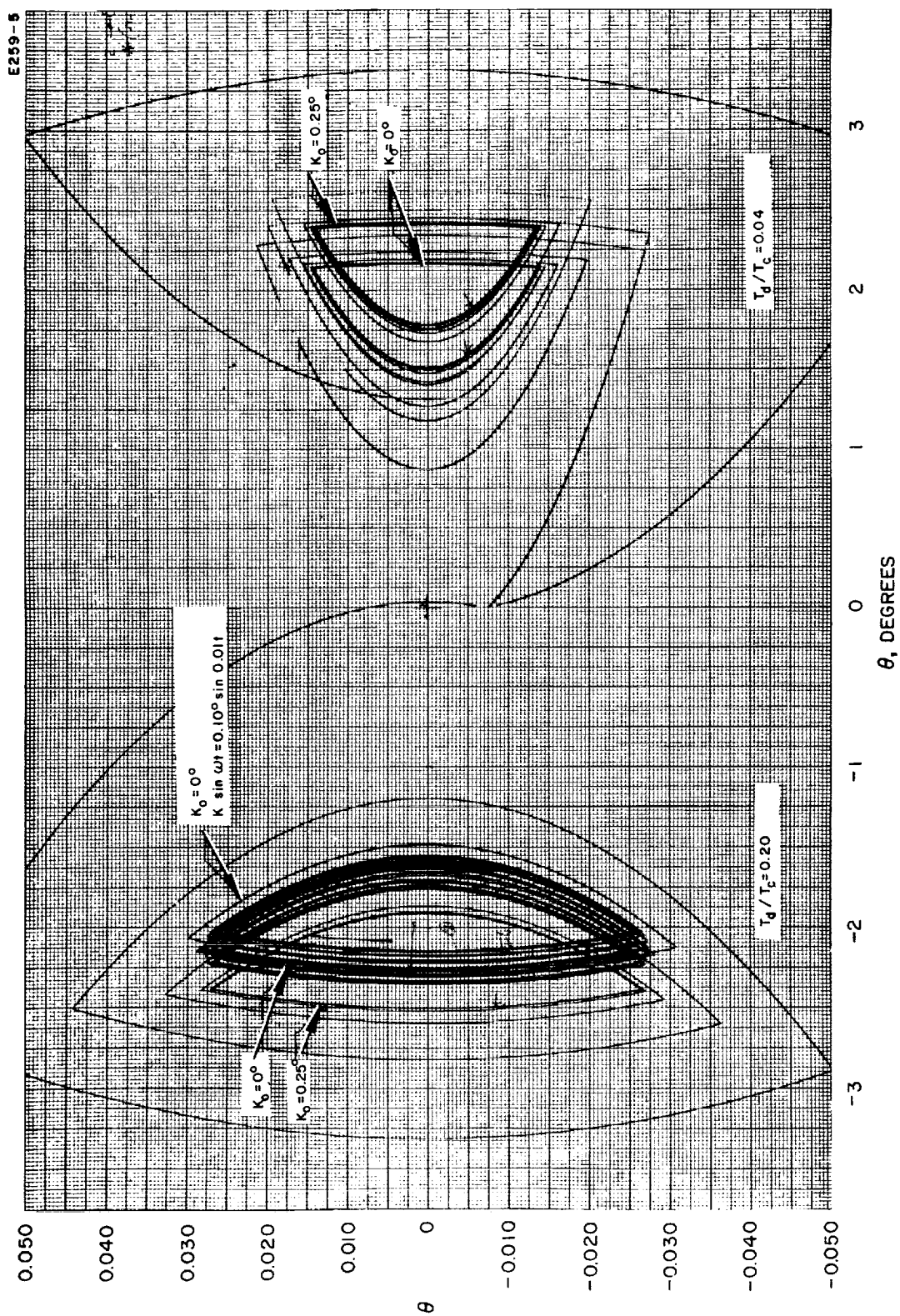
77

Fig. 33. Phase plane plots showing the effect on system performance caused by various combinations of null shift, sinusoidal null drift, and disturbance torque to control torque ratio (zero noise).

The addition of a sinusoidal null drift, K_2 sin ωt = 0.10 degree sin .01 t to the system for T_d/T_c = 0.2 is illustrated by the dark line phase trajectories on the left of Figure 33. Again, as in the disturbance torque-free case, the null drift input appears as noise and causes a bounded phase trajectory motion about the nominal limit cycle. Neither the limit cycle rates nor the power figures of merit differ significantly from the ideal limit cycle.

The addition of sensor white noise, $n(t)$ = 0.025 degree rms, is illustrated in Figure 34 by the phase trajectories on the left. The outer limit cycle represents the noise-free case for T_d/T_c = 0.04 and the inner trajectories represent the effect of noise additicn. The white noise inputs are seen to reduce the "average" phase trajectory rate from the noise-free case (a similar effect was noted for T_d = 0); however, for T_d = 0, this effect increases rather than decreases the average power figure of merit. The range of average power figures of merit becomes approximately 122.5 watts to 174.3 watts as compared with the nominal of 115.9 watts in the noise-free case.

The addition of sinusoidal null drift and noise to the system is illustrated by the phase trajectories on the right of Figure 34 for T_d/T_c = 0.04 and by Figure 35 for T_d/T_c = 0.20. In each case, the trajectories vary somewhat more from cycle to cycle than in the drift-free case, but the long term boundedness and stability are apparent in each case. The null drift is 0.1 degree sin .01 t for both examples.

(6)   Effect of Sensor Gain Variation

Sensor gain was varied from 0.5 to 1.7 and the effect was a contraction or expansion of the nominal (K_s = 1.0) phase plane trajectories. Figure 36 illustrates this effect for T_d = 0, the limit cycles for K_s = 1.20, 1.0, 0.8, and 0.6 being those of increasing size. The limit cycle rates for these cases increase slightly from .0152 deg/sec for K_s = 1.2 to .0187 deg/sec for K_s = 0.6, while

Fig. 34. Phase plane plots showing the effect on system performance caused by white noise and a sinusoidal null drift when the ratio of disturbance torque to control torque is 0.04.
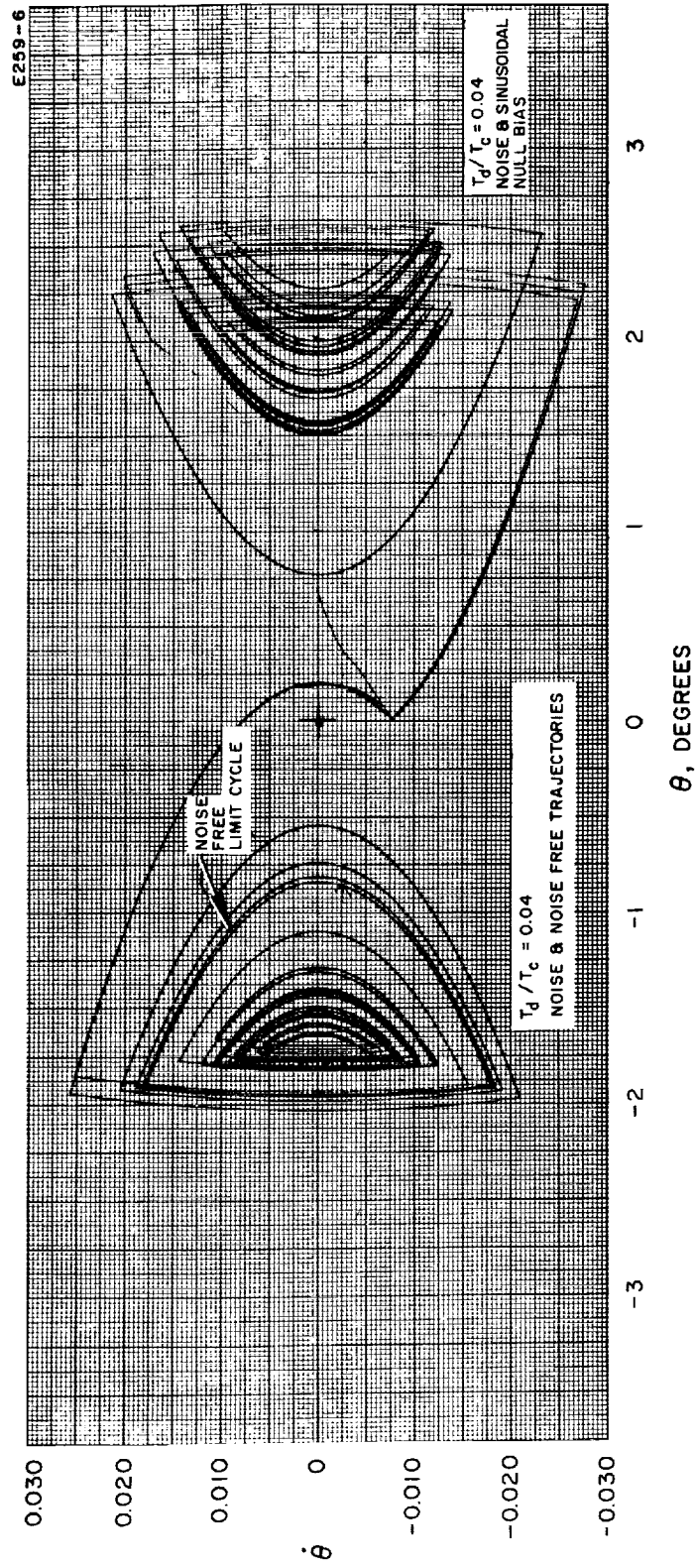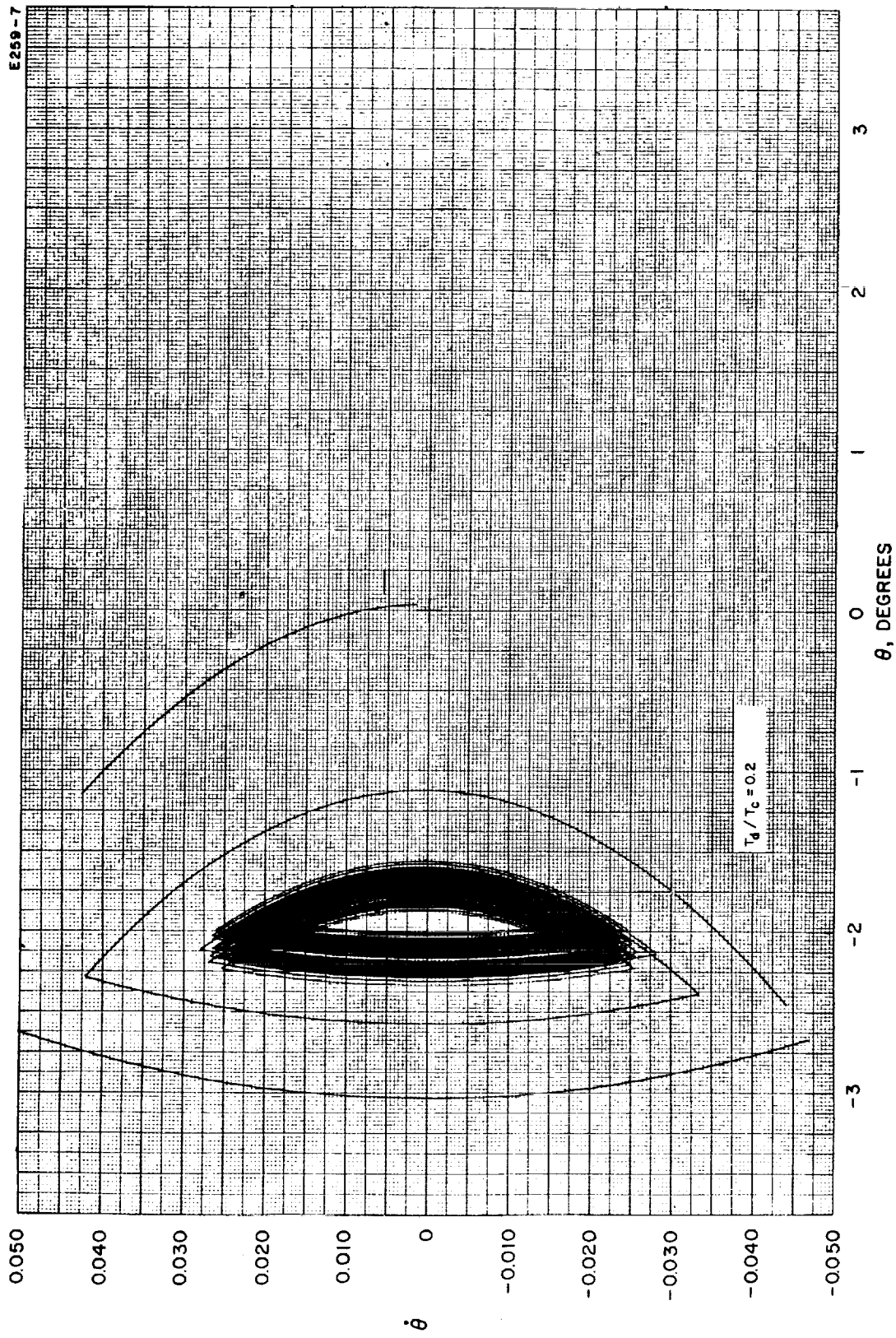
Fig. 35.   Phase plane plots showing the effect on system performance caused by white noise and a sinusoidal null drift when the ratio of disturbance torque to control torque is 0.2.
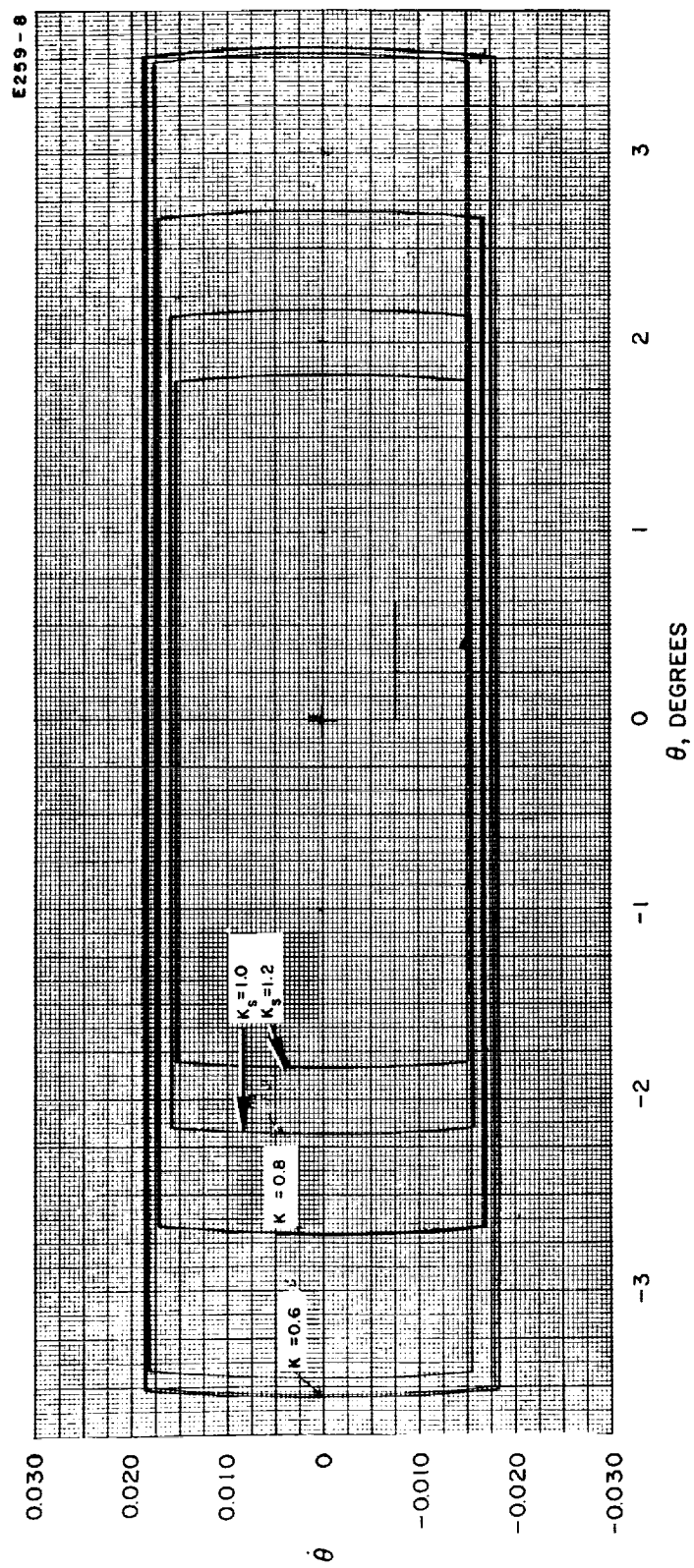
81

Fig. 36.   Phase plane plots showing the effect on system performance caused by variation in sensor gain (zero disturbance torque).

82

the deadband excursion increases from ± 1.90 degrees for $K_s = 1.2$ to ± 3.60 degrees for $K_s = 0.6$.

A similar variation of K_s was performed for the noise-free case where $T_d/T_c = 0.04$, and the results are illustrated by the phase trajectories on the right of Figure 37. The limit cycles going from left to right represent gains of 1.7, 1.0, 0.9, 0.7, and 0.5, respectively. In each case, the limit cycle is expanded or contracted slightly, depending upon whether the gain is less than or greater than one, respectively. The significant effect of gain change is the shifting of the excurtion of the phase trajectory. For the case of $K_s = 1.7$, the maximum excursion is 1.0 degree, while for $K_s = 0.7$, the excursion is 3.25 degrees.

System performance with particular values of all nonlinear sensor characteristics is shown by the phase trajectories on the left of Figure 37 and in Figure 38 ($T_d = 0$). The parameters of each trajectory are summarized in Table VI. The results indicate acceptable system performance for rather severe values of the sensor parameters. Although succeeding cycles of Figure 38 are quite unlike, this is attributed to the large amplitude (1.0 degree) of the sensor null drift, and the long term stability is demonstrated.

TABLE VI

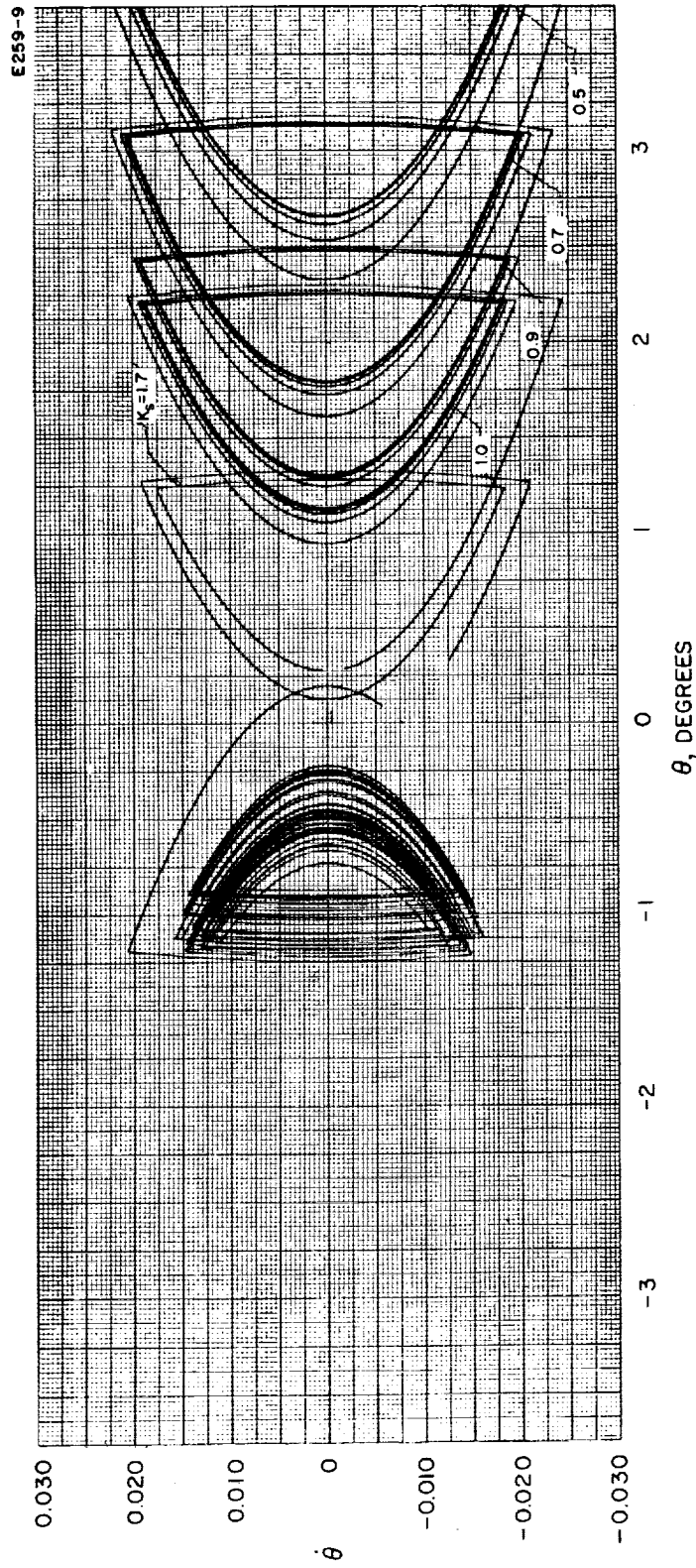|	Figure 37	Figure 38
T_d/T_c	0.04	0
K_o	0.25 degree	0.25 degree
K_1	0.25 degree	1.0 degree
ω	.01 rad/sec	.001 rad/sec
K_s	1.70	1.20
n (t)	0.025° rms	0.025° rms
Sensor response	$1/(.1s + 1)$	$1/(.1s + 1)$
Filter	$1/(.11s + 1)^2$	$1/(.11s + 1)^2$

Fig. 37. Phase plane plots showing the effect on system performance caused by: (1) variation in sensor gain when the ratio of disturbance torque to control torque is 0.04 (right side) and (2) a selected set of values of nonlinear sensor characteristics (left side).
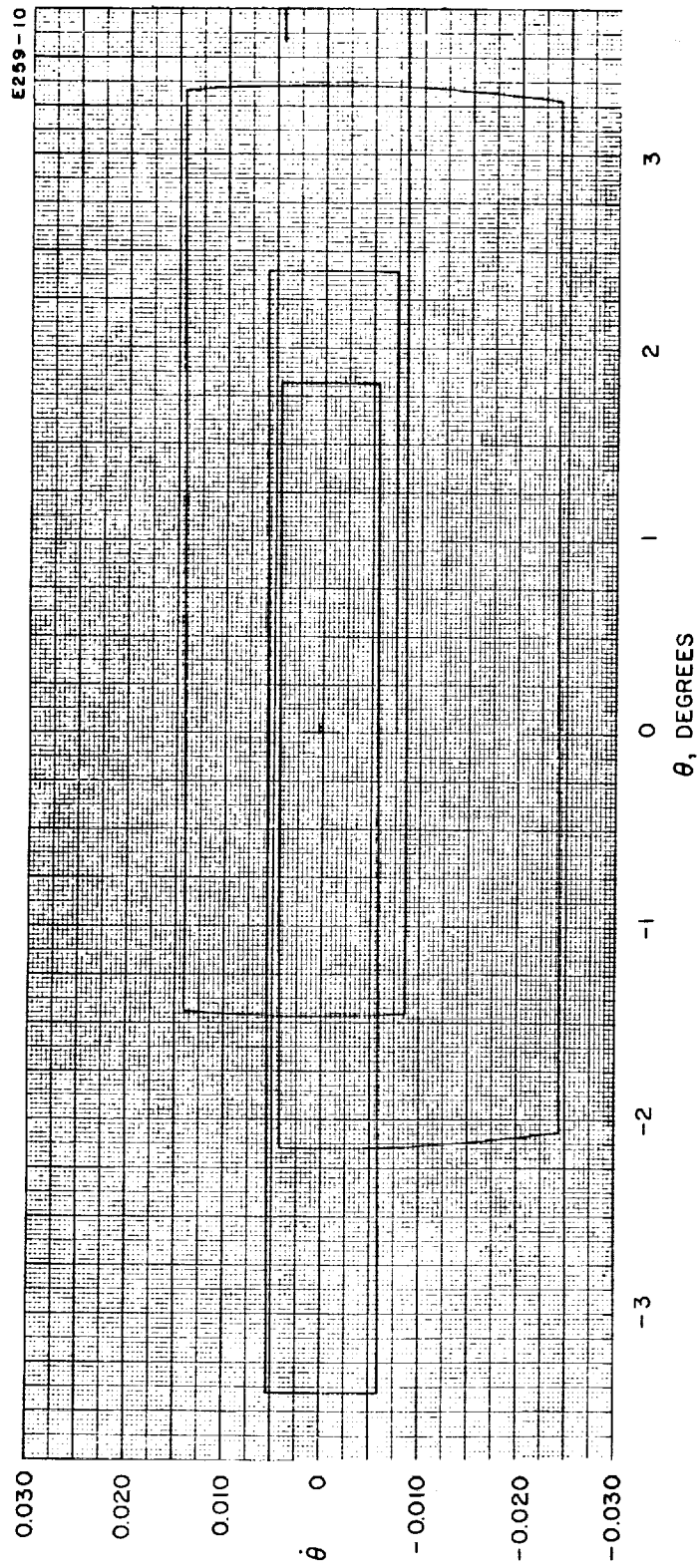
84

E259-10

Fig. 38. Phase plane plot showing the effect on system performance caused by a selected set of values of nonlinear sensor characteristics.

85

(7)   Low Altitude System Simulation Conclusions

The results of the analog simulation for the low altitude mission indicate acceptable system performance under the influence of wide ranges of sensor characteristic parameters such as noise, null shift and drift, gain variation, and vehicle disturbance torque. Qualitatively, the effect of each parameter may be summarized as follows:

1) Noise improves performance in the hard limit cycle and slightly degrades performance in the soft limit cycle due to a decreased length of control torque application.

2) Constant sensor null shift only shifts the limit cycle angular amplitude without affecting the limit cycle rate or the average power figure of merit.

3) Sinusoidal sensor null drift behaves essentially as low frequency noise, causing a wider variation of phase trajectories from cycle to cycle, but not degrading seriously either average power or limit cycle rate. Large amplitude drifts (1.0 degree) will cause the angular amplitude to vary to a large extent from the nominal switching point.

4) Gain variation essentially expands or contracts the phase trajectory along the angle axis without seriously degrading average power.

5) Disturbance torques increase the average power consumption (by increasing duty cycle) and in the presence of noise, average power is increased somewhat more than the noise-free case due to the reduction of the control torque application time.

For the range of vehicle parameters simulated for the mission, the conclusion is reached that acceptable system performance in this mission may be expected, even in the presence of adverse sensor characteristics. Quantitative evaluation of the

slight system performance degradation that was observed can be obtained once the actual sensor characteristics are obtained as a result of laboratory and flight tests.

B.   Synchronous Orbit Mission Analog Simulation

The purpose of the high altitude mission simulation was to determine the necessary noise filtration as a function of the sensor white noise inputs. This simulation was identical with phase one of the preliminary low altitude simulation as reported in References 1 and 11. Detailed noise information was not generally available on proposed high altitude attitude sensors since most candidate sensors have not been fabricated or tested to date.

(1)   Description of Simulated System

The major difference between the preliminary low altitude simulation and the preliminary high altitude simulation is the change of vehicle parameters such as inertia, control moment arm, and attitude accuracy.

Table VII summarizes the parameters utilized in the high altitude simulation. The parameters are based upon the system analyzed in Reference 13. The block diagram of Figure 25 represents the high altitude simulated system, provided that sensor null shift, null drift, gain change, and disturbance torques are neglected.

TABLE VII

θ_d	$\pm$ 0.5 degree
λ	1.0×10^{-5} rad/sec^2
P_c	25.0 watts
d_s P_s	32.0 watts
P_T	160 watts
P_w T_w	0.75 watt-hr.
τ_1	23.755 sec.
τ_2	1.735 sec.

TABLE VII
(contd.)

h_o	.02 degree
h_1	0.5 degree
τ	10 sec.
τ_{dl}	30.0 sec.

Due to the different hysteresis and smaller control acceleration for the high altitude control system, the nominal noise (and noise filter) free limit cycle angular rate will be of smaller magnitude than for the low altitude case (.003 deg/sec compared with .010 deg/sec). This effect along with smaller hysteresis and switch-kick amplitude will essentially reduce the allowable noise input amplitude to the switch which controls the ionizer warm-up command. Hence, for a given sensor white noise rms input, a greater degree of noise filtration will be required for the high altitude mission than for the low altitude mission. (A more complete discussion of these effects is given in References 1 and 11.)

(2)   Results of Synchronous Orbit System Simulation

The results of the high altitude simulation may be summarized by Figure 39 in which the required noise filtration corner frequency ω_3 is plotted as a function of input noise rms amplitude. By comparison with Figure 15 of Reference 1 (noise filtration required for low altitude mission), it can be seen that for a fixed rms noise input, more noise filtration is required for the high altitude mission. Stated in another way, less noise will be tolerable from the high altitude attitude sensor than from the low altitude sensor if the amount of degrading (from a power sense) noise filtration is to be the same in both cases. Noise filtration for the high altitude mission has been limited to either first or second order filters in order to minimize the amount of electronic complexity required.
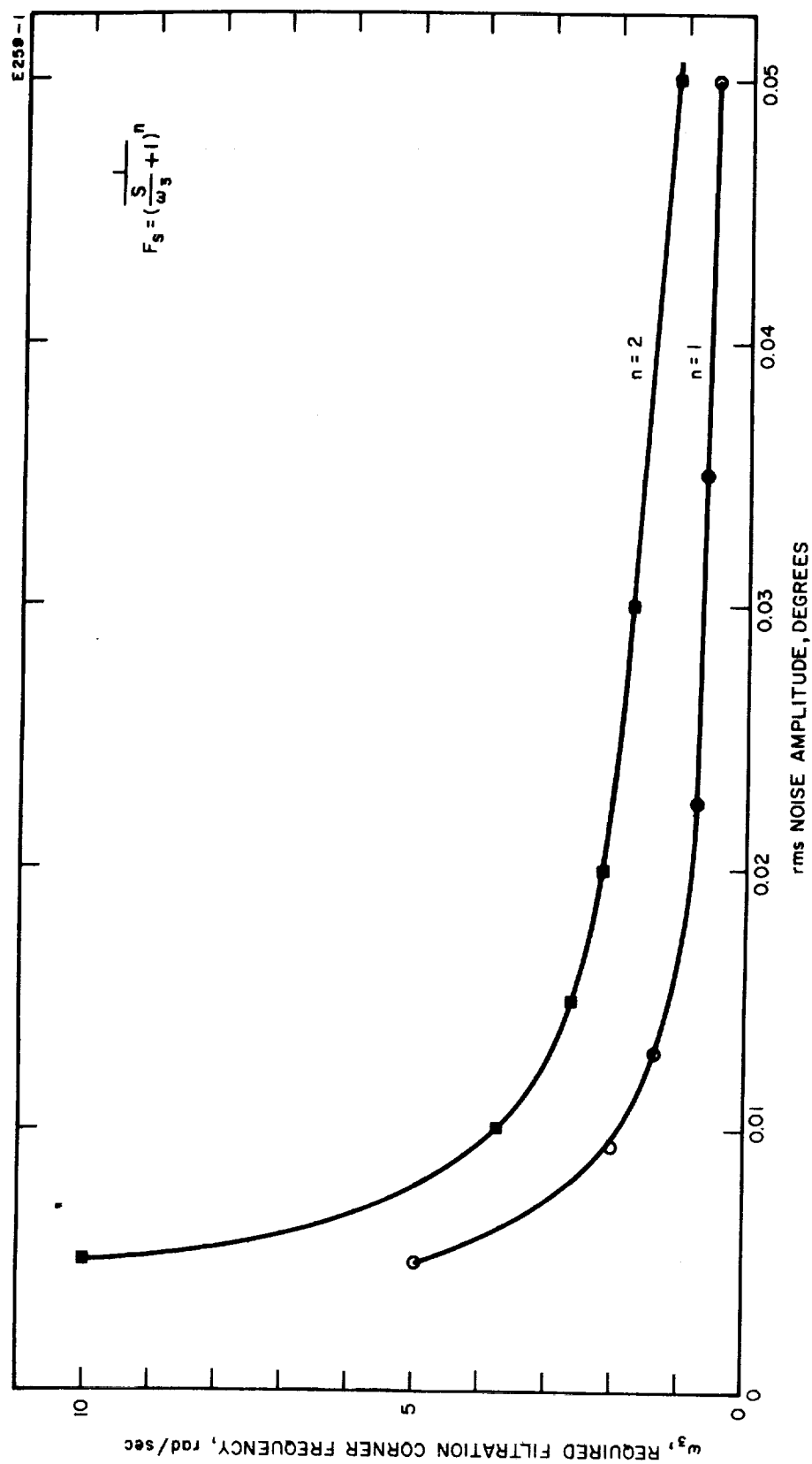
Fig. 39. Noise filtration corner frequency as a function of input noise rms amplitude for a synchronous orbit mission.

The corresponding average power figures of merit for the high altitude mission are shown in Figure 40. These average powers were computed upon the basis of no disturbance torque and no noise, with the system operating with the sensor response characteristics (τ_s = 0.1 sec) and the particular values of required noise filtration. These average powers should be compared with a nominal average power of 95.3 watts (Reference 13), for a warm-up energy of 0.75 watt-hr and an attitude deadband of $\pm$ 0.5 degree.

(3)   Synchronous Orbit System Simulation Conclusions

The results of the high altitude simulation as represented in Figures 39 and 40 may be utilized as similar results were utilized for the low altitude preliminary simulation; that is, to aid in the selection of a sensor candidate and to adequately filter sensor noise of a particular sensor in order to determine system performance due to other effects. The over-all system performance under the influence of sensor characteristics such as null shift and drift, gain variation, and disturbance torques can be expected to be quite similar to that for the low altitude mission. Hence, the conclusions drawn from the final low altitude simulation should also be applicable to the high altitude mission, once the appropriate noise filtration is selected.
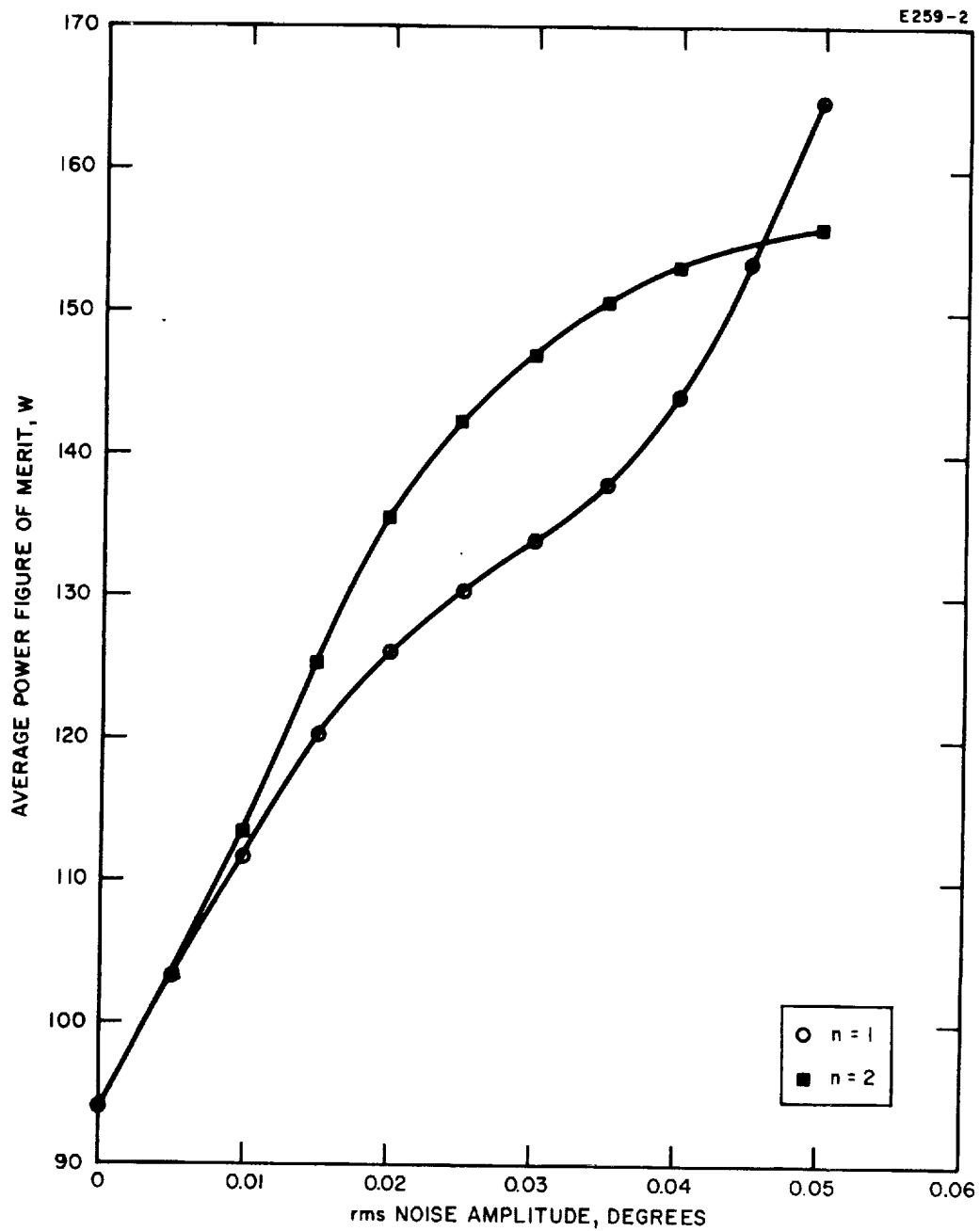
Fig. 40. Average power figure of merit as a function of input
noise rms amplitude for a synchronous orbit mission.

IV.   Conclusions

The sensor survey has indicated that a suitable attitude
sensor subsystem may be obtained to satisfy the requirements of
the ion engine system for attitude control and station keeping of a
synchronous orbit satellite. The results show that while the
attitude error requirements may be entirely satisfied, a savings
in sensor subsystem complexity may be realized if the pitch,
roll, and yaw attitude excursion limits are increased to ± 1.3
degrees (i.e., standby pitch and roll gyros and the yaw compen-
sation function generator may be eliminated).

The system simulation study has indicated the acceptable
performance of the attitude control system when the expected
characteristics of sensors are employed in the simulation. For
the range of vehicle and sensor parameters simulated (which
covers a practical range for the hardware design), it has been
demonstrated that the attitude control system stability is accept-
able and that the degradation of system performance (i.e.,
increase in duty cycle and power consumption) with non-ideal
attitude error signals is held within acceptable limits.

93

REFERENCES

1. Hughes Research Laboratories, Preliminary Report,
    SERT-III Mission Sensor Survey Study, Contract
    NAS 3-2510, May 1963.

2. Robertson, Robert E., Gravity Gradient Determination of
    The Vertical, ARS Journal, Vol. 31, No. 11, p. 1509.

3. Heppner, J. P., et al, Explorer X Magnetic Field Results,
    NASA TN D-1669, p. 169, May 1963.

4. Hughes Aircraft Company Proposal, Attitude Sensors for
    Use with Ion Rocket Engine System for Attitude Control and
    Station Keeping, Feb. 1963.

5. Santa Barbara Research Center Report 2070-2, Relative
    Detector Response to the Irradiance from Stars, G. Hyde
    and G. Plount, May 1962.

6. Bendix Corp., Eclipse-Pioneer Division Proposal No. 7321-
    63-9, Polaris Star Sensor, May 1963.

7. ITT Federal Laboratories, Technical Proposal for One-Axis
    Polaris Star Sensor, May 1963.

8. Santa Barbara Research Center Proposal SM-7-63, June 1963.

9. Barnes Engineering Co. Proposal BEC-P530, High Accuracy
    Horizon Sensor for Synchronous Satellites, July 1962.

10. Kearfott Proposal, Earth Sensor for Synchronous Orbits, April 1963.

11. IDC 2242/2228, "Results of Preliminary Analog Simulation
    for Low Altitude Ion Engine Mission," from R. J. McElvain,
    dated 22 May 1963.

REFERENCES

(contd)

12. Hughes Research Laboratories Quarterly Progress Report
     No. 2, Contract NAS 3-2510, dated 18 April 1963.

13. IDC 2242/1562, "Summary of Ion Engine System Performance
     Tradeoff Analysis," from R. J. McElvain, dated 21 November
     1962.